공학박사 학위논문

A study on supercapacitor and thermocell based on phase transitional ionic liquid

상변화성 아이오닉 리퀴드를 기반으로한 슈퍼커패시터와 열전 소자에 관한 연구

2022 년 8 월

서울대학교 대학원

재료공학부

박 진 우

A study on supercapacitor and thermocell based on phase transitional ionic liquid

상변화성 아이오닉 리퀴드를 기반으로한
슈퍼커패시터와 열전 소자에 관한 연구

지도 교수 선 정 윤

이 논문을 공학박사 학위논문으로 제출함
2022 년 8 월

서울대학교 대학원
재료공학부
박 진 우

박진우의 공학박사 학위논문을 인준함
2022 년 8 월

위 원 장 장 호 원 (인)

부위원장 선 정 윤 (인)

위 원 김 진 영 (인)

위 원 이 지 석 (인)

위 원 이 지 훈 (인)

Abstract

With the rapid development of society and industry, the demand for unprecedented energy is increasing. In order to supply energy to meet the demand, various types of energy supply methods have been studied. First, energy storage system (ESS) is a charge / discharge type energy supply device, which is usually applied to a field requiring a large amount of energy. A supercapacitor is a representative ESS. In the ion solution electrolyte in the supercapacitor, an electric double layer is formed by charging and energy is stored. Next, the self-generated energy supply device is applied to a field that has relatively little energy but requires continuous energy supply. An ionic thermocell is a typical self-generated energy supply device. Thermoelectric is generated due to a difference in ion concentration at both electrodes according to a temperature gradient. However, the ion solvent electrolyte applied to these devices has issues in evaporation and chemical stability. Therefore, ionic liquids that have chemical stability and very low vapor pressure are being evaluated as next-generation materials.

Here, we demonstrate that ionic liquids are promising materials to be introduced into electrolytes of supercapacitors and thermocells. Particularly, it is possible to dramatically control the ionic conductivity at their melting point by preparing electrolytes through phase-transitional ionic liquids. These electrolytes make it possible to design energy supply devices that show new functions or improved performance. Two energy supply devices with a phase-transitional ionic liquid electrolyte were explored; phase-transitional supercapacitor and thermocell

In first part, selective operation supercapacitors were demonstrated by introducing phase-transitional ionogel as electrolyte into supercapacitor. Supercapacitors with excellent physical stability was manufactured through gelation of ionic liquid. The phase transitional characteristic of the ionic liquid made them possible to selectively operate by distinguishing the operating mode and storage mode. Furthermore, they showed long-term energy storage by effectively suppressing the self-discharge of the supercapacitor in the storage mode. The selective operating supercapacitor is expected to expand their used in environments with high temperatures or large temperature variation such as a desert or space industry.

In second part, the high seebeck coefficient of the ionic thermocell was demonstrated through the phase transitional ionic liquid. The mechanism of a thermoelectric phenomenon due to the phase difference occurring at both electrode was introduced. It was shown that the seebeck coefficient could change or obtain a high value depending on the phase difference. Furthermore, it was demonstrated that the Seebeck coefficient was significantly improved by the phase difference in all phase transitional ionic liquids. It is expected that the enhanced thermogalvanic cell due to the phase difference has advanced the commercialization of the thermoelectric device by proposing a novel mechanism for the study of thermoelectric effect improvement, which is still in early stage.

Keyword : phase transition, ionic liquid, supercapacitor, thermocell

Student Number : 2016-26947

Table of Contents

Abstract i

List of Figures vi

List of Tables xiv

Chapter 1. Introduction 1

1.1 Study background 1

1.1.1 Supercapacitor 1

1.1.2 Thermocell 2

1.1.3 Ionic liquid 3

1.1.4 Goals and outline of this dissertation 3

Chapter 2. Phase-transitional ionogel-based supercapacitors for a selective temperature operation 7

2.1 Introduction 7

2.2 Experimental section 9

2.2.1 Fabrication of SCs 9

2.2.2 Ionogel analysis 10

2.2.3 Characterization of supercapacitor electrochemical properties 11

2.2.4 Self-discharging test 11

2.3 Results and Discussion 12

2.3.1 Phase-transitional characteristics of the ionogel 12

2.3.2 Selective operation of SCs in operating mode and storage mode 21

2.3.3 The capacitive performance of SCs in operating mode. 31

2.3.4 Self-discharge characteristic of SCs in storage mode 36

2.4 Conclusion 45

Chapter 3. The Enhancement of Ionic Thermoelectric Seebeck Coefficient by Phase Difference 46

3.1 Introduction 46

3.2 Experimental section 48

3.2.1 Fabrication of the thermogalvanic cell 48

3.2.2 Ionic liquid analysis 49

3.2.3 Characterization of thermogalvanic cell thermoelectrical properties 49

3.3 Results and Discussion 50

3.3.1 A thermoelectric enhancement mechanism induced by phase difference 50

3.3.2 Properties of the ionic liquid in different phases 54

3.3.3 Thermoelectric performance of $[AMIM]^+[Cl]^-$ based thermogalvanic cell 61

3.3.4 Thermoelectric performance of other phase transitional ionic liquid 67

3.4 Conclusion 71

Chapter 4. Conclusion 72

References 72

Abstract in Korean.....84

Curriculum Vitae 87

List of Figures

Figure 1.1 Schematic illustration of a supercapacitor.

Figure 1.2 Schematic illustration and mechanism of a thermogalvanic cell.

Figure 2.1 Phase transition of $[EMIM]^+[NO_3]^-$ / PAAm ionogel. (a) Schematic illustration of phase transition of $[EMIM]^+[NO_3]^-$ IL in a PAAm network. The ion movement is suppressed or activated based on temperature-triggered phase transformation of ionic liquid (IL) in the ionogel. (b) Structural formulas of phase-transitional IL ($[EMIM]^+[NO_3]^-$), and monomer (PAAm) and crosslinker (PEGDA) miscible with the IL.

Figure 2.2 (a) Differential scanning calorimetry (DSC) curves of pure $[EMIM]^+[NO_3]^-$ IL and $[EMIM]^+[NO_3]^-$ / PAAm ionogel. (b) X-ray diffraction (XRD) patterns of $[EMIM]^+[NO3]^-$ ionic liquid at 25 ℃ and 45 ℃. Peaks in the XRD pattern indicate that the ionic liquid form crystal lattices at 25 ℃, while peaks are not observed at 45 ℃ due to decrystallization of the ionic liquid.

Figure 2.3 (a) UV-VIS spectra of the ionogel at 25 ℃ and 45 ℃. Transmittance of the ionogel was shifted from 1 % to 99 % under 25 ℃ of ambient temperature. (b) Photographs of ionogels under 45 ℃ and 25 ℃ of ambient temperature. Ionogel containing excited IL exhibited soft and transparent while ionogel containing crystallized IL exhibited rigid and opaque.

Figure 2.4 Fourier-transform infrared spectroscopy (FT-IR) spectrum of freeze-dried polyacrylamide, pure ionic liquid at 25 °C, ionogel at 25 °C and 45 °C.

Figure 2.5 (a) Stress-strain curves of ionogel at 25 ℃ and 45 ℃. The inset shows the stress strain curve of ionogel at 45 ℃. (b) Tensile cyclic stress-strain curves of ionogel at 45 ℃ up to the strain of 100 %. (c-h) Various sequential mechanical deformations of the ionogel at 45 ℃. Before deformation, stretching, Twisting, Folding, Rolling and after deformation.

Figure 2.6 (a) Decrystallized ionogel at 45 ℃ And crystallized ionogel at 25 ℃. The volume change during the phase transition does not occur. (b) Photographs of ionogel after 50 cycles of repeated crystallization-decrystallization. A geometry of the ionogel with 20 mm in length, 20 mm in width and 0.5 mm in thickness was fabricated. Any optical scattering caused by phase separation was not observed in the gel during 50 cycles.

Figure 2.7 Fabrication process of phase-transitional SCs.

Figure 2.8 (a) SEM images of ionogel/electrodes interface of the SCs. A highly porous surface of the carbon electrode was observed. When the ionogel was polymerized on the carbon electrode, interface of the ionogel and the electrode was robustly bonded. (b) SEM image of ionogel membrane cross-sections at various magnifications.

Figure 2.9 (a) Electrochemical impedance spectroscopy (EIS) curves of a storage mode of supercapacitor (SC_{SM}) and an operating mode of supercapacitor (SC_{OM}). Resistance of the SCs under ambient temperature of RT was 161 kΩ and (b) dramatically decreased up to 3 Ω with phase transition of the ionogel at 45 ℃

Figure 2.10 Electrochemical performance of ionogel electrolyte based supercapacitor. (a) Cyclic voltammetry (CV) curves of SCs under ambient temperature from 25 ℃ to 50 ℃. (b) Specific capacitance of a supercapacitor at different temperatures. The operating mode and storage mode was separated by the phase transition.

Figure 2.11 Electrochemical performance of pure ionic liquid electrolyte based supercapacitor. (a) Cyclic voltammetry (CV) curves of supercapacitor under temperature from 25 ℃ to 50 ℃. (b) Specific capacitance of a supercapacitor at different temperatures

Figure 2.12 Reversibility of capacitance according to the temperature cycles; Red dot: 45 ℃, blue dot: 25 ℃.

Figure 2.13 Real-time phase transition of SC. After lowering the temperature from 45 ℃ to 25 ℃, the phase transition started after 1 min and crystallization was completed after 2.5 min.

Figure 2.14 Electrochemical performance of phase-transitional SCs in operating mode. (a) Cyclic voltammetry curves of SC_{OM} at different scan rates from 12.5 to 200 mV s^{-1}. (b) Galvanostatic charge/discharge curves and (c) specific capacitance at current densities of 0.2, 0.5, 1, 2, 4 A g^{-1}

Figure 2.15 (a) A Ragone plot of the power density versus energy density for SC_{OM}. (b) Cyclic stability of SC_{OM} under applied current density of 0.5 A g^{-1}. Inset is charge-discharge cycles at first ten and final ten stages.

Figure 2.16 Cyclic voltammetry curves of SC_{OM} under bending deformation. Softness of the SCs and robust interface of electrode/ionogel led stable electrochemical performance.

Figure 2.17 Schematic illustrations of charging and self-discharging processes of SC_{SM} and SC_{OM}. Self-discharge was described with a diffusion-controlled model.

Figure 2.18 Galvanostatic charge/discharge (GCD) curves at current density of 0.02 A g^{-1}.

Figure 2.19 Self-discharging curves of a SC at 45 ℃ and 25 ℃. (c) A self-discharging curve of a supercapacitor at 25 ℃. The curve is fitted by the diffusion-controlled model. The measured diffusion parameter m is 7.16×10^{-4} V $s^{-1/2}$.

Figure 2.20 (a) A self-discharging curve of a supercapacitor at 25 ℃. The curve is fitted by the diffusion-controlled model. The measured diffusion parameter m is 7.16×10^{-4} V $s^{-1/2}$. (b) A self-discharging curve of a supercapacitor at room temperature (25 ℃) fitted by a ohmic leakage model. (c) A self-discharging curve of a supercapacitor at 45 ℃ fitted by a diffusion-controlled model. The measured diffusion parameter m is 2.68×10^{-3} V $s^{-1/2}$.

Figure 2.21 (a) LED is operated at a current of 100 ~ 200 μA and a voltage of 2 V by a DC power supply (KEYSIGHT, E36233A) and LED operation by a charged $SC_{SM.}$ (b, c) Suppressed self-discharging of the SC enhances optical power duration of a green LED during a discharging process.

Figure 3.1 In conventional thermoelectric cells, when a temperature difference occurs between electrodes, an electric potential is generated through redox reaction of

chloride ions. The mobility of Cl- anions steadily increases with increasing temperature.

Figure 3.2 Different-phase thermoelectric cells result in higher potentials due to the increased mobility of chloride ions induced by the different phases between the low and high temperature electrodes. In the solid phase, chloride ion movement is inhibited by the lattice structure, whereas in the liquid ion movement is free. As the phase changes from solid to liquid, the mobility of chloride ions increases rapidly. As a result, there is a large difference in the interaction between the chloride ions and the electrode at both temperatures, which enhances the thermoelectric effect.

Figure 3.3 (a) Optical micrographs and picture of $[Amim]^+[Cl]^-$ at low and high temperaturesAt 30°C, the ionic liquid exists as a solid and the crystal structure is observed, but at 60°C, since the ionic liquid exists as a liquid, nothing is detected. Scale bar, 100 μm. (b) A chemical structure of the $[Amim]^+[Cl]^-$ crystal with space group P21/c (a= 7.931, b=12.836, c=16.452 Å, β= 96.22°)

Figure 3.4 (a) DSC curve of the $[Amim]^+[Cl]^-$, heating from -50 to 80 ℃. The melting point of the $[Amim]^+[Cl]^-$ is shown as 53.1 ℃. (b) Transmittance of $[Amim]^+[Cl]^-$ in the visible light region with a wavelength of 300 to 800 nm at both temperatures. $[Amim]^+[Cl]^-$ ionic liquid showed no permeability at 30 ℃, while the ionic liquid shows similar permeability to that of the yellow filter at 60 ℃. (c) X-ray diffraction curve of the $[Amim]^+[Cl]^-$ ionic liquid at 30 and 60 ℃. The crystallized $[Amim]^+[Cl]^-$ shows the XRD peaks at 30 ℃ while the decrystallized $[Amim]^+[Cl]^-$ presents no XRD peaks at 60 ℃.

Figure 3.5 The schematic illustration of electrochemical impedance spectroscopy (EIS) measurements.

Figure 3.6 The nyquist plots of the thermoelectric cell at (a) 30 and (b) 60 ℃. The inset of the plot shows the equivalent circuit of EIS system.

Figure 3.7 The schematic illustration and picture of thermogalvanic cell. A clearly distinct phase is observed depending on the temperature.

Figure 3.8 Seebeck coefficients of [Amim]+[Cl]- according to different phase states. The solid-solid and liquid-liquid phase thermogalvanic cells exhibit Seebeck coefficients of 0.83 and 1.83 mV/K, respectively, and the solid-liquid thermogalvanic cells exhibit improved Seebeck coefficients of 3.33 mV/K.

Figure 3.9 (a) Power-voltage-current (*P-V-I*) characteristics of thermogalvanic cell with different phase state. In the heterogeneous state, the maximum power is dramatically improved. (b) Stability of thermogalvanic cells over time. In the heterogeneous phase, the OCV was stable for more than 50 hours.

Figure 3.10 (a) Seebeck coefficient depending on cell length. The change of Seebeck coefficient with the change of cell length was insignificant. (b) Generation voltage of thermoelectric cells connected in series. The voltage increased proportionally to the number of cells.

Figure 3.11 The chemical structures of the phase-transitional ionic liquid; $[HOEtMIM]^+[Cl]^-$, $[EMIM]^+[Cl]^-$ and TBAC.

Figure 3.12 Seebeck coefficient of phase transition ionic liquids depending on temperature range. All ionic liquids exhibit improved Seebeck coefficients in a homogeneous state.

List of Tables

Table 2.1 Self-discharge performance of ionic liquid-based SCs.

Table 3.1 The values of D, μ, n of $[AMIM]^+[Cl]^-$ IL based electrolyte.

Chapter 1. Introduction

1.1 Study Background

1.1.1 Supercapacitor

An Energy Storage System (ESS) is defined as a device capable of storing energy and power. A supercapacitor is one of the ESS that bridge the gap of energy and power between batteries and conventional capacitors [1]. Supercapacitors (SCs) can handle very high current rates, and are characterized by very high power density and long cycle lifetime [2, 3]. Consisting of two porous electrodes, separator and ionic solvent electrolyte, SCs store charge by electrostatic adsorption of electrolyte ions onto the surface of the oppositely charged electrodes [4] (Figure 1.1). The surface capacitance of capacitor is described by following formula:

$$C = \frac{\varepsilon}{d} A \qquad (1)$$

where C is the capacitance, ε is the permittivity, A is the electrode surface area and d is the thickness. In the case of SCs, high capacitance is derived due to the large surface area of the porous electrode and the thin thickness of electric double layer. In order to manufacture SCs with better performance, it is important to properly select each component of SCs. Among them, electrolyte is key to designing safe and high performance SCs. In order to meet the required functions and performance, various types of electrolytes have been studied [5].

1.1.2 Thermocell

As the Internet of Things (IoT) market continues to grow, a suitable type of energy supply is required. In order to be applied to IoT, a relatively small, but a self-generated energy supply device is needed. A thermocell is one of self-generated energy supply devices, and generates electricity through a temperature gradient between electrodes. A thermogalvanic cell is a type of thermocell in which thermal energy is converted into electrical energy via a redox process occurring at the electrodes and ions in the ion solvent electrolyte [6] (Figure 1.2). This is a thermodynamically driven process, based upon the entropy difference of the redox couple. As shown by the equation (2), a temperature gradient (ΔT) across two electrodes generates a potential difference (ΔV) due to the entropy difference, and this is quantified as the Seebeck coefficient (S) [7].

$$S = \frac{\Delta V}{\Delta T} \tag{2}$$

However, the redox based thermocell has a relatively low Seebeck coefficient. Therefore, studies have been conducted to improve the Seebeck coefficient by various methods such as crystallization [8, 9] and synergistic thermodiffusion and thermogalvanic effects [10] .

1.1.3 Ionic liquid

Appropriate selection of ion solvent electrolyte is essential to fabricate devices with desired functions and performance. However, conventional ion solvent electrolytes have problems with solvent evaporation and chemical stability. An ionic liquid (IL) represents a compound composed of ions having a melting point of less than 100°C [11], and is attracting attention as an alternative to the existing solvent. Additionally, ILs are characterized by very low vapor pressure, high thermal stability, high ionic conductivity and electrochemical stability [12]. These features make ILs suitable to be used as an electrolyte in energy supply devices such as supercapacitor [13], battery [14] and thermocell [15]. Especially, ionic liquids that have a melting point at room temperature have a characteristic of undergoing phase transition at their melting point. The phase change allows us to control the movement of ions dramatically beyond the temperature-driven method. By applying them to a device that operates through the flow of ions, it is possible to develop into a device with enhanced performance or versatility. Therefore, our research contributes to the development of new methods to meet the increasing demand for energy supply devices.

1.1.4 Goals and outline of this dissertation

Purpose of this dissertation is to demonstrate that phase-transitional ionic liquids are promising materials to be introduced into electrolytes of energy supply devices. This dissertation is composed of two parts.

In Chapter 2, a supercapacitor was fabricated based on the phase transitional ionogel. When the temperature is elevated from 25 °C to 45 °C, resistivity of the gel is decreased from 2318.4 kΩ·cm to 43.2 Ω·cm. At the same time, the capacitance is boosted from 0.02 to 37.35 F g^{-1} and this change was repeatable. The phase transition can switch the SCs from 'operating mode' to 'storage mode' when the temperature drops. A degree of self-discharge is greatly suppressed in the storage mode, storaging 89.51 % of charges after 24 hours in self-discharge tests.

In Chapter 3, a thermogalvanic cell based on chloride redox reaction were demonstrated. In conventional thermoelectric cells, when a temperature difference occurs between electrodes, an electric potential is generated by redox reaction of chloride ions. On the other hand, by using the phase-change ionic liquid, the thermoelectric cells with different phases have a higher difference in the mobility of chloride ions induced by the different phases between the cold electrode and the hot electrode, resulting in a high potential. The fabricated galvanic cell reached the Seebeck coefficient value of 3.33 mV/K, which significantly increased the Seebeck coefficient compared to homogeneous, only by the phase difference without any addition.

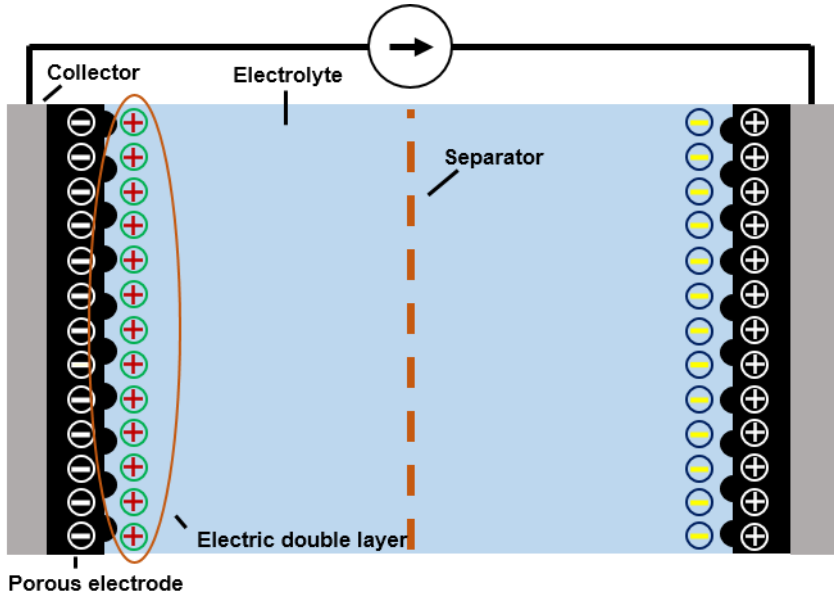

Figure 1.1 Schematic illustration of a supercapacitor.

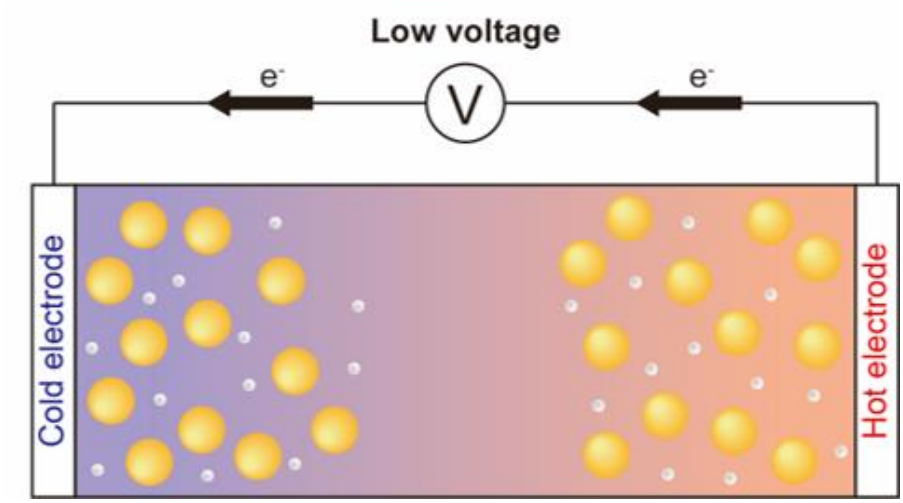

Figure 1.2 Schematic illustration and mechanism of a thermgalvanic cell.

Chapter 2. Phase-Transitional Ionogel-based Supercapacitors for a Selective Operation

2.1 Introduction

With the rapid development of society and the emergence of new industries, the ever-increasing demand of energy has increased a need for more efficient energy storage systems. Electric double layer capacitors (EDLCs), also known as supercapacitors (SCs), are representative electrochemical energy storage systems that meet these needs. SCs are electrostatically charged through charge separation at both of the high-surface area porous electrode/electrolyte interfaces[16]. They can be charged/discharged in a short period of time and are capable of withstanding a few thousand cycles[17]. These properties allow SCs to be used in vehicles, portable electronics and military sectors[18] wherever there is a need to release a large amount of stored energy in a short time. However, SCs have a very high self-discharge, making them difficult to sustain a state of charge for a long time. Therefore, various factors have been studied to reduce the self-discharge[19]. One of the main factors of the self-discharge is movement of ions in the electrolyte. In order to control ion mobility, electrodes with stronger interactions with ions are developed[20], or separators[21] and additives[22, 23] were combined with electrolytes to suppress the movement of the ions. However, the self-discharge of SCs basically occurs because ions are always activated in the electrolyte. Therefore, it is expected that the self-

discharge of the SCs can be effectively lowered if the movement of ions is deactivated when the SCs are not used.

A phase transition is a method that dramatically changes the flow of ion with temperature. Since ions are crystallized or decrystallized depending on the phase, the movement of ions can be easily controlled according to the temperature. One of the ionic materials that can undergo a phase transition at ambient temperature is an ionic liquid. Ionic liquids (ILs) refer to compounds composed of ions with melting points below 100℃[11] and some ILs change phase at their melting point. By using a phase-transitional ionic liquid, it is possible to dramatically change mobility of ions[24]. Additionally, ILs are characterized by very low vapor pressure, high thermal stability, high ionic conductivity and electrochemical stability[12]. These features make ILs suitable to be used as an electrolyte in a SC and various studies have been conducted based on them[25, 26]. Based on these characteristics, by applying phase-transitional ILs to SCs as electrolytes, it is expected that the activation degree of SCs can be controlled according to the temperature. That is, when the temperature elevated above the melting point, SCs become active and are operated as an energy source. On the other hand, SCs become inactive state by lowering the temperature to suppress the movement of ions. In the inactive state, SCs are able to store the energy for a long time.

Here, we have fabricated phase-transitional ionogel-based supercapacitors for a selective operation. The electrolyte was made of ionogel using a phase-transitional

ionic liquid as a solvent. Through a gelation, various disadvantages of liquid electrolytes such as electrolyte leakage, corrosion and packaging problems[27] could be overcome. The ionogel was fabricated from acrylamide (AAm) monomer with phase-transitional ionic liquid, 1-Ethyl-3-methylimidazolium nitrate $[EMIM]^+[NO_3]^-$, as the ionogel solvent. The fabricated supercapacitor can be activated by elevating the temperature above the melting temperature, called an 'Operating mode'. After operation, the SC can be converted into a 'Storage mode' by lowering the temperature, where self-discharge is reduced and there is no energy consumption to maintain energy storage. Since the ionogel electrolyte is stable even at a high temperature and can be selectively activated, we expect that supercapacitors can be used in environment with high temperatures or with large temperature variation such as a desert or a space industry.

2.2 Experimental section

2.2.1 Fabrication of SCs.

Carbon electrodes were prepared by coating aluminum foil with a mixture of activated carbon power (Sigma, C9157), Super P (Wellcos) and Poly(vinylidene fluoride) (PVDF, Wellcos , #7300) in a ratio of 8:1:1. Ionogel solution was synthesized by mixing 12 wt% acrylamide (AAm, Sigma, A8887) to provide monomers for the polymer network, $[EMIM]^+[NO_3]^-$ (Iolitec, IL-0005-HP) as the ionogel solvent, 2.5

wt% poly(ethylene glycol) diacrylate (PEGDA; Sigma, 455008) as a crosslinker and 0.4 wt% 2-Hydroxy-4′-(2-hydroxyethoxy)-2-methylpropiophenone (Irgacure 2959, Sigma, 410896) as a photoinitiator. The ionogel solution was stirred for one hour at 70 ℃ to create a homogeneous solution before polymerization. For preparation of the SCs, electrodes and a 1 mm-thick PDMS (Sylgard 184) mold were attached to Teflon tape to provide a flexible substrate. Then, the solution was poured into the PDMS mold and encapsulated with the same substrate. The solution was cured at a wavelength of 365 nm for one hour to obtain phase-transitional ionogel-based SCs.

2.2.2 Ionogel analysis.

Ionogels were prepared in the same manner without the substrate. The transmittance of each ionogel sample was measured over a wavelength range of 300 to 400 nm using UV-VIS spectroscopy (Agilent Technologies, Cary 60). Differential scanning calorimetry (DSC) was carried out using a TA Instruments Discovery DSC. The samples were analyzed at a heating rate of 2 °C min^{-1} over a temperature range of -20 °C to 100 °C. Mechanical tensile tests were performed to measure the mechanical property of ionogel. A geometry of the sample with 30 mm in length, 10 mm in width and 2 mm in thickness was used. The specimens were mounted to a tensile machine (Instron, 3343) and were stretched with a 50 N capacity load cell at a stretch rate of 10 mm s^{-1}. The initial length of the specimen between the grips was 5mm. The fourier-transform infrared spectroscopy (FT-IR) (Thermo Scientific, Nicolet iS 10 Spectrometer) was carried out to analysis spectrums of freeze-dried polyacrylamide, pure $[EMIM]^+[NO_3]^-$ ionic liquid, ionogel at 25 °C and 45 °C with wavenumbers from

550 cm^{-1} to 4000 cm^{-1}. The cross section of a supercapacitor was characterized by a scanning electron microscope (SEM) (Carl Zeiss, AURIGA) at an accelerating voltage of 2 kV.

2.2.3 Characterization of supercapacitor electrochemical properties.

The performance of ionogel-containing SCs that were 18 mm in length, 8 mm in width and 1mm in thickness was evaluated using a two-electrode system. Electrochemical impedance spectroscopy (EIS), cyclic voltammetry (CV) and stability tests were carried out using a potentiostat/galvanostat (Gamry Reference 600+) with a two-electrode-system at various temperatures on a hot plate. The EIS test was performed in the frequency range of 0.1 Hz – 1 MHz. The CV test was performed in the potential range of 0 – 2 V at various scan rates (12.5, 25, 50, 100, 200 mV s^{-1}). The galvanostatic charge/discharge (GCD) curves were measured using the multichannel electrochemical workstation (ZIVE, MP1) at various current densities of 0.2, 0.5, 1, 2, and 4 A g^{-1} in a potential window of 0 – 2 V. The stability of SCs was measured by subjecting them to 3000 cyclic charge-discharge cycles in the potential range of 0 – 2 V at a current density of 0.5 A g^{-1} to measure capacitance retention.

2.2.4 Self-discharging test.

The supercapacitor was charged to 1.85 V with a current density of 0.02 A g^{-1} and held at this terminal voltage for 2 h at 45 ℃ to ensure the fully charging. The open circuit voltage (OCV) was measured for 24 hours in two cases of SC at room temperature (25 ℃) and 45 ℃. To demonstrate usability of SCs, they were charged

to 2 V for 2 hours at 45 ℃ and solidified by lowering the temperature. After that, they were connected to LED lights (LUG30243/G-C, 155 Ω, ICbanQ). The photos of the LED light were recorded and the light powers of the LED were measured using the optical power meter (Newport, 1919-R). LED experiments and measurements were conducted in a dark room.

2.3 Results and Discussion

2.3.1 Phase-transitional characteristics of the ionogel

The characteristics of the synthesized ionogel electrolyte for the phase-transitional SCs are illustrated in Figure 2.1a. Acrylamide monomers became polyacrylamide and formed a 3-D matrix in the ionic liquid through chemical crosslinking with PEGDA when induced by the photo-initiator. Below the melting point, the ionic liquid ions are crystallized. Therefore, the movement of ions is suppressed. When the temperature is raised above the melting point of the ionic liquid, the ionic liquid ions are decrystallized, allowing the ions to move freely. The structural formulas of the phase-transitional ionic liquid, $[EMIM]^+[NO_3]^-$, polyacrylamide (PAAm) and PEGDA constituting the ionogel electrolyte are shown in Figure 2.1b. All components are miscible with the ionic liquid to form a homogeneous solution. DSC measurements were carried out to investigate the phase transition temperature of pure $[EMIM]^+[NO_3]^-$ IL and $[EMIM]^+[NO_3]^-$ / PAAm ionogel. (Figure 2.2a). The DSC

results show that the melting point of the ionic liquid is 44.7 ℃, while that of the ionogel is 44.8 ℃. To observe the crystallization – decrystallization change of ionic liquid according to the phase, X-ray Diffraction (XRD) analysis was conducted (Figure 2.2b). The data exhibits a clear difference in crystallinity at 25 ℃ and 45 ℃. To precisely observe changes in transparency in the visible region, the transmittance of the 1 mm-thick ionogel was measured in the wavelength range of 400 to 800 nm using spectroscopy (Figure 2.3a). According to the transmittance spectra, the crystallized ionogel shows very low transmittance of less than 10%, while the decrystallized ionogel shows high transmittance of more than 90%. Below the melting point, a phase-transitional ionic liquid is known to form a crystal lattice[24]. Therefore, the difference in transmittance is the result of crystallized – decrystallized motion of ionogel as the phase transition depending on the temperature. In order to compare the state of the ionogel at different temperatures, an ionogel sample with a size of 10 X 10 X 2 mm^3 was prepared (Figure 2.3b). At room temperature (25 ℃), the ionogel was crystallized and appeared to be rigid and opaque, while the decrystallized ionogel at 45 ℃ exhibited transparent and flexible. To analyze the chemical compositions of ionogel, we have carried out the fourier-transform infrared spectroscopy (FT-IR) of polyacrylamide, pure $[EMIM]^+[NO_3]^-$, ionic liquid at 25 ℃, ionogel at 25 ℃ and 45 ℃ (Figure 2.4). In the spectrum of ionogel, adsorption peaks located at 3387 cm^{-1} and 1683 cm^{-1} were assigned to the N–H stretching and C=O stretching on polyacrylamide. The yellow and green regions (3140 ~ 3055 cm^{-1} and 2971 ~ 2883 cm^{-1}) are assigned to the sp^2 C-H stretching and sp^3 C-H stretching, respectively. The peak located at 1332 cm^{-1} are attributed to the N=O stretching of nitrate ion. The

bands located at 1575cm^{-1}, 1635 cm^{-1} and 1172 cm^{-1} are assigned to C=N stretching vibration, C=C stretching and C-N stretching vibration of the imidazole ring, respectively[28]. The peak near 1172 cm^{-1} of polyacrylamide is attributed to the C-O stretch of the PEGDA crosslinker. It is confirmed that peaks of ionogel at 25 ℃ is similar to ionic liquid at 25 ℃, while ionogel at 45 ℃ is similar to polyacrylamide in yellow and green regions. To investigate the mechanical properties of the ionogel, stress-strain tensile tests were carried out. Figure 2.5a shows the stress-strain curves of ionogel according to temperature. The crystallized ionogel exhibits rigid physical properties by showing an elastic modulus value of 40.8 MPa and an elongation of 15 %, whereas decrystallized ionogel exhibits soft physical properties by showing an elastic modulus value of 26.9 kPa and an elongation of 272%. The tensile cyclic stress-strain curve of ionogel up to the strain of 100 % at 45℃ shows little physical deformation during 500 cycles, demonstrating high robustness (Figure 2.5b). Furthermore, by applying various sequential mechanical deformations to the ionogel, it was verified that the ionogel is sufficiently robust (Figure 2.5c-h). Since polymers usually undergo rapid degradation, changes in electrochemical performance according to phase transition were considered[29, 30]. During the phase transition, negligible volume change was observed (Figure 2.6a). Moreover, the uniform distribution of ionic liquid ions did not change during repeated phase transitions (Figure 2.6b). Therefore, the electrochemical performance degradation of the electrolyte during phase transition caused by the volume change and ion distribution change did not occur.

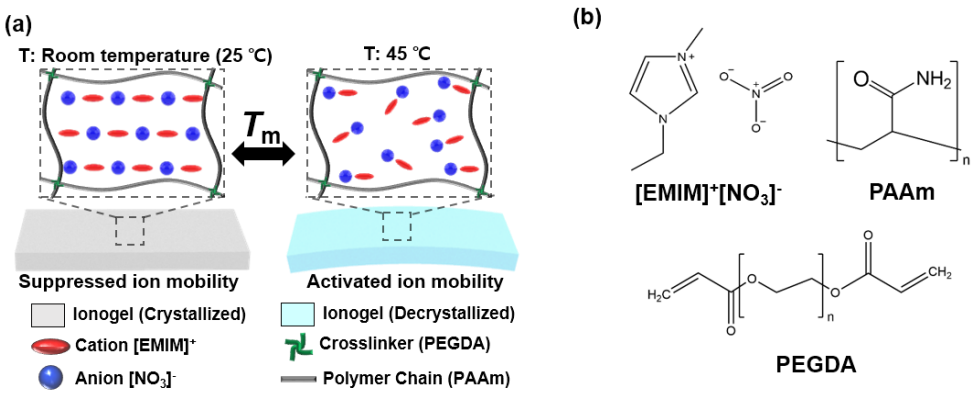

Figure 2.1 Phase transition of $[EMIM]^+[NO_3]^-$ / PAAm ionogel. (a) Schematic illustration of phase transition of $[EMIM]^+[NO_3]^-$ IL in a PAAm network. The ion movement is suppressed or activated based on temperature-triggered phase transformation of ionic liquid (IL) in the ionogel. (b) Structural formulas of phase-transitional IL ($[EMIM]^+[NO_3]^-$), and monomer (PAAm) and crosslinker (PEGDA) miscible with the IL.

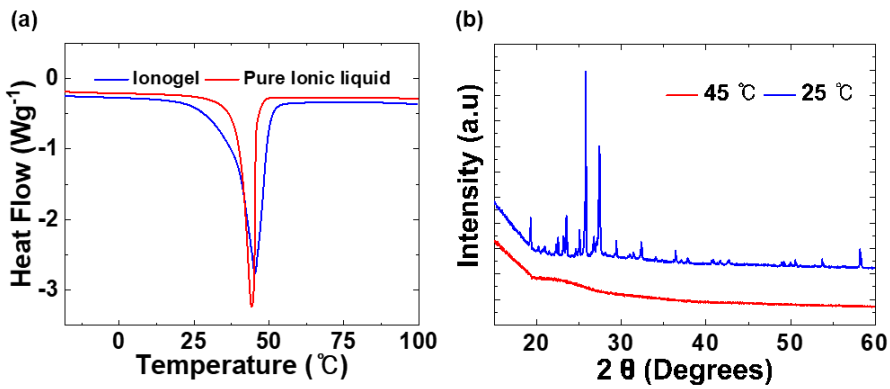

Figure 2.2 (a) Differential scanning calorimetry (DSC) curves of pure $[EMIM]^+[NO_3]^-$ IL and $[EMIM]^+[NO_3]^-$ / PAAm ionogel. (b) X-ray diffraction (XRD) patterns of $[EMIM]^+[NO3]^-$ ionic liquid at 25 ℃ and 45 ℃. Peaks in the XRD pattern indicate that the ionic liquid form crystal lattices at 25 ℃, while peaks are not observed at 45 ℃ due to decrystallization of the ionic liquid.

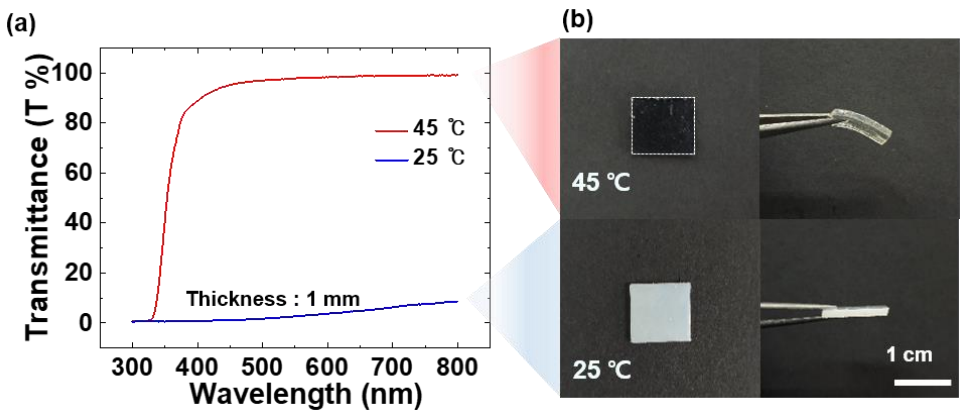

Figure 2.3 (a) UV-VIS spectra of the ionogel at 25 ℃ and 45 ℃. Transmittance of the ionogel was shifted from 1 % to 99 % under 25 ℃ of ambient temperature. (b) Photographs of ionogels under 45 ℃ and 25 ℃ of ambient temperature. Ionogel containing excited IL exhibited soft and transparent while ionogel containing crystallized IL exhibited rigid and opaque.

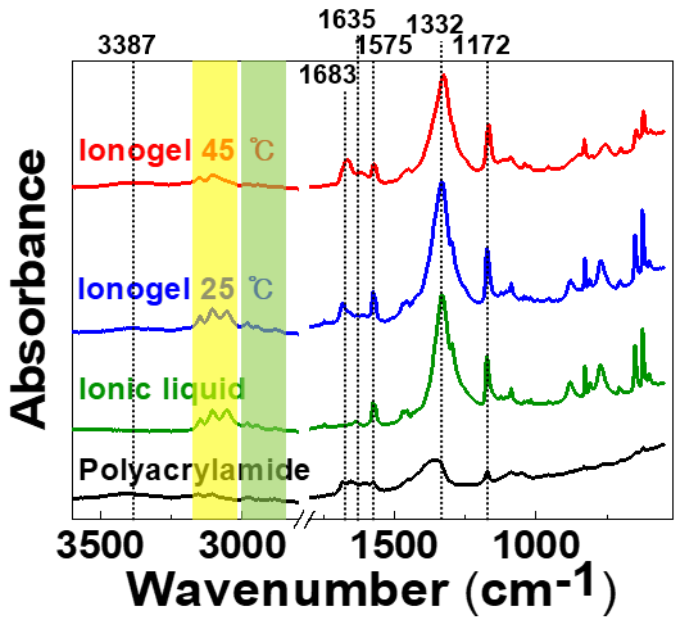

Figure 2.4 Fourier-transform infrared spectroscopy (FT-IR) spectrum of freeze-dried polyacrylamide, pure ionic liquid at 25 °C, ionogel at 25 °C and 45 °C.

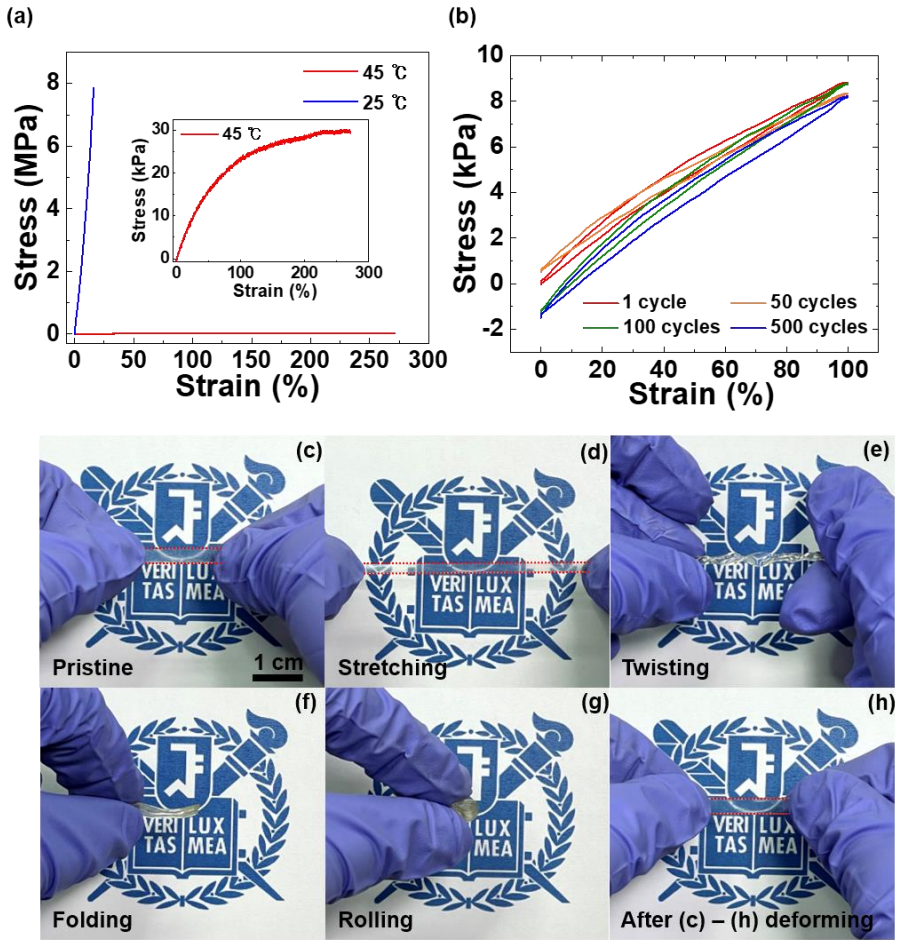

Figure 2.5 (a) Stress-strain curves of ionogel at 25 ℃ and 45 ℃. The inset shows the stress strain curve of ionogel at 45 ℃. (b) Tensile cyclic stress-strain curves of ionogel at 45 ℃ up to the strain of 100 %. (c-h) Various sequential mechanical deformations of the ionogel at 45 ℃. Before deformation, stretching, Twisting, Folding, Rolling and after deformation.

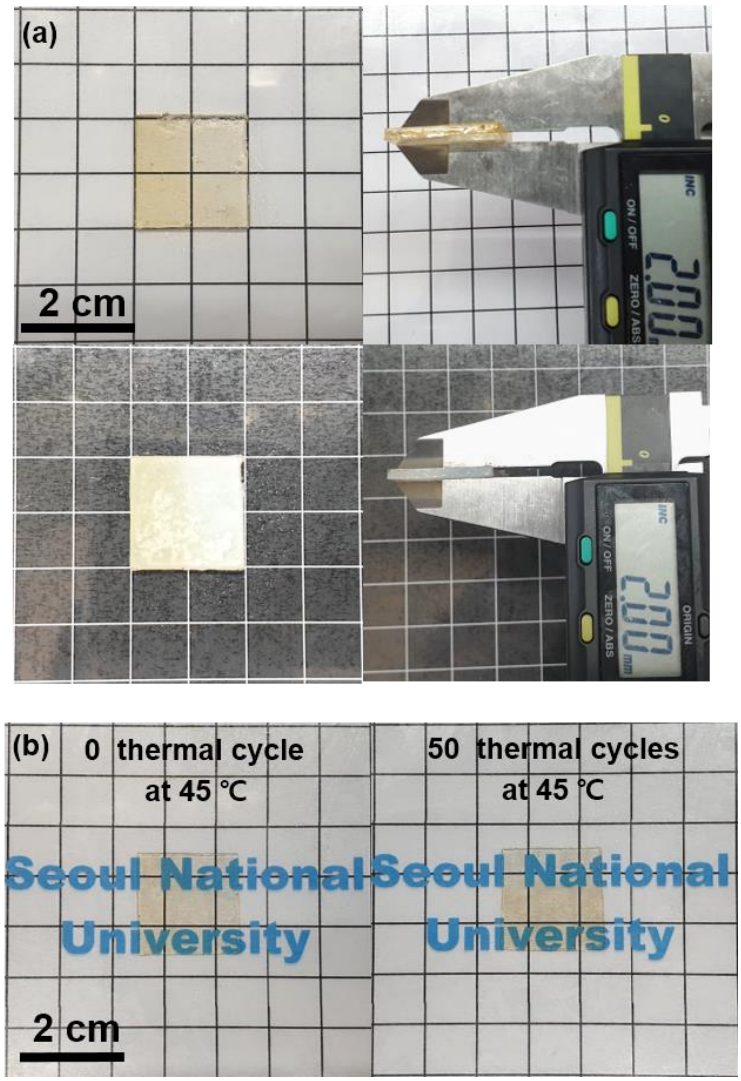

Figure 2.6 (a) Decrystallized ionogel at 45 ℃ And crystallized ionogel at 25 ℃. The volume change during the phase transition does not occur. (b) Photographs of ionogel after 50 cycles of repeated crystallization-decrystallization. A geometry of the ionogel with 20 mm in length, 20 mm in width and 0.5 mm in thickness was fabricated. Any optical scattering caused by phase separation was not observed in the gel during 50 cycles.

2.3.2 Selective operation of SCs in operating mode and storage mode.

We synthesized phase-transitional SCs based on the $[EMIM]^+[NO_3]^-$ ionogel electrolyte with carbon electrodes. The SCs fabrication process is illustrated in Figure 2.7. SCs were composed of Teflon tape as a flexible and moisture proofing substrate, aluminum foil as a current collector, carbon electrodes, PDMS mold and ionogel electrolyte. The PDMS mold served as a framework for fabrication of bulky ionogel and prevented substrate separation when the SCs were bent. When manufacturing the ionogel electrolyte, in-situ polymerization was performed to ensure perfect bonding between the electrode and the surface of the electrolyte[31] so that the bonding surface did not deviate during phase transition or bending. Figure 2.8a shows cross-sectional SEM images of the electrolyte/electrode surface. The image of the carbon electrode without ionogel revealed a highly porous carbon surface. When the ionogel electrolyte was added, a strongly bonded surface of ionogel and carbon electrode was observed. To observe the porous polymer network, the ionic liquid of the ionogel was replaced with deionized water for 3 days and freeze dried. Then, SEM images of the cross section of the dried ionogel were taken (Figure 2.8b). We classified SCs into an Operating Mode of Supercapacitor (SC_{OM}) and Storage Mode of Supercapacitor (SC_{SM}) according to the phase of the ionogel electrolyte. Figure 2.9a,b show the Nyquist plots for SC_{OM} and SC_{SM}. The plots reveal a semicircle at high frequencies, a non-vertical line at intermediate frequencies and a sloping line at low frequencies. The diameter of the semicircle is assigned to the sum of the electrolyte resistance in

the porous electrode and the electrode resistance[32]. The measured resistivity values were 2318.4 kΩ·cm and 43.2 Ω·cm for SC_{SM} and SC_{OM}, respectively, for a difference of about 53,600 times. Peculiarly, SC_{SM} showed a large non-vertical line following the semicircle with a value of 835.2 kΩ·cm. This tendency seems to be due to the large diffuse layer resistance in the solid phase[33]. Due to this dramatic difference in resistance, the activation-deactivation of the SCs is determined by temperature. The CV curve was derived to evaluate the performance of the phase-transitional SCs (Figure 2.10a,b). The SCs were measured at various temperatures (25 and 35, 40, 45 and 50 °C) at a scan rate of 50 mV s^{-1}. The CV curves show that SCs perform very poorly at 25 and 35 °C. They are activated as the temperature approaches the melting point and become fully operational above the melting point of 41.3 °C. It is also showed that the SCs are very stable at a high temperature of 50 °C. These results are confirmed by the specific capacitance values at different temperatures. The specific capacitance derived from CV tests using a two-electrode system is determined by eqn (3); where C_m (F g^{-1}) is the specific capacitance, m is the mass of active materials, v is the scan rate, I is the discharge current and ΔV (V_{high}-V_{low}) is the scanned potential window.

$$C_m = \frac{1}{mv\Delta V}\int_{V_{low}}^{V_{high}} IdV \tag{3}$$

At 25 and 35 °C, specific capacitances are almost zero (0.02 and 1.04 F g^{-1}, respectively). As the temperature is gradually increased, the solid and liquid phases coexist

at 40 °C, resulting in a specific capacitance of 22.57 F g^{-1}. Finally, the specific capacitance exceeds 37.35 F g^{-1} above the melting point. To compare the electrochemical performance of the pure ionic liquid electrolyte-based supercapacitor, a similar supercapacitor, but with an $[EMIM]^+[NO3]^-$ ionic liquid electrolyte was fabricated, and the electrochemical performance was measured (Figure 2.11a,b). Since the ionogel is mostly composed of ionic liquid, ionic liquid based SCs exhibit similar performance to ionogel based SCs. To confirm that the activate/deactivate motion of the SCs is repeatable and evaluate the cycling life, the specific capacitances were measured by deriving the CV curve 50 cycles at 25 and 45 °C at a scan rate of 50 mV s^{-1}. Then, the capacitance retention was calculated based on the specific capacitance value at the first cycle at 45 °C, as shown in Figure 2.12. Active/inactive motions are clearly observed during several cycles, and capacitance retention was decreased about 10 % after 45 cycles. Figure 2.13 shows the real-time phase transition of the SC. The temperature of SC_{OM} at 45 °C was lowered to 25 °C. In the ionogel electrolyte of SC, the phase transition began after 1 minute and crystallization was fully completed after 2.5 minutes.

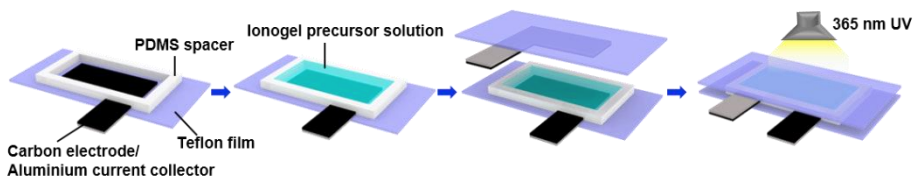

Figure 2.7 Fabrication process of phase-transitional SCs.

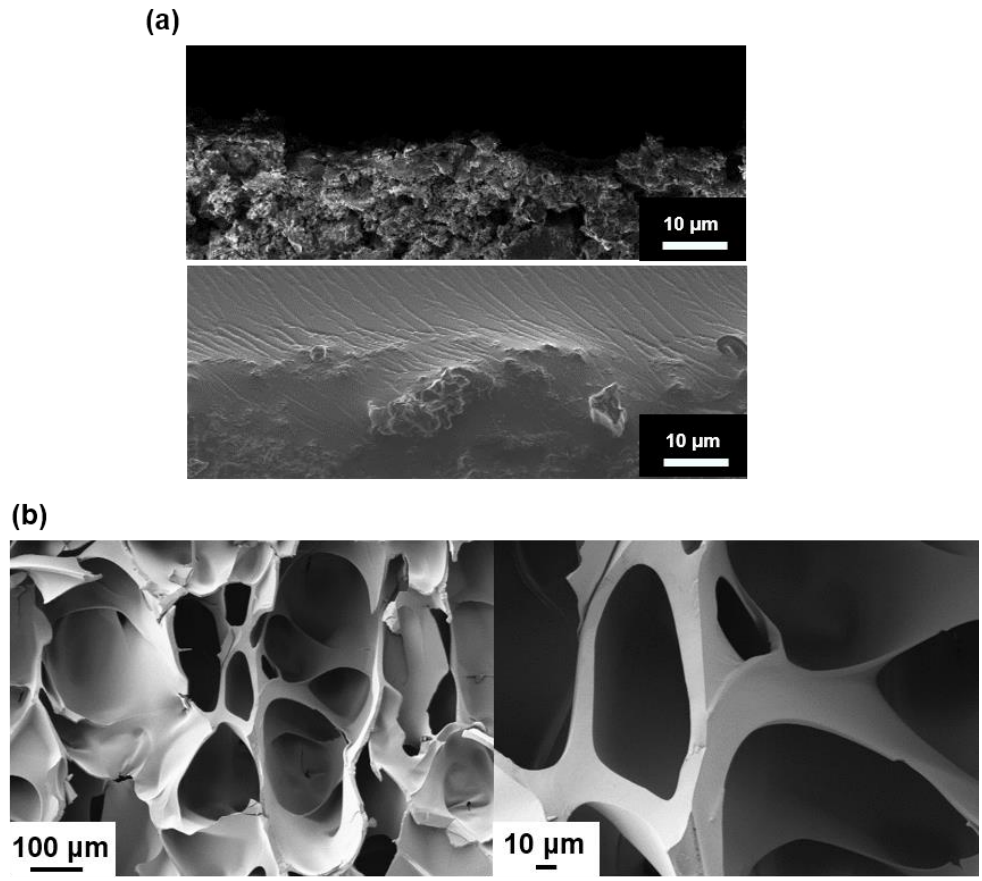

Figure 2.8 (a) SEM images of ionogel/electrodes interface of the SCs. A highly porous surface of the carbon electrode was observed. When the ionogel was polymerized on the carbon electrode, interface of the ionogel and the electrode was robustly bonded. (b) SEM image of ionogel membrane cross-sections at various magnifications.

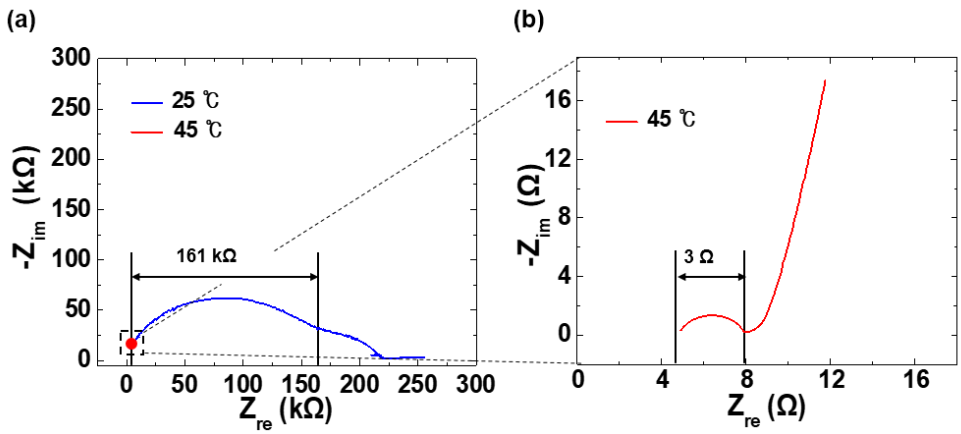

Figure 2.9 (a) Electrochemical impedance spectroscopy (EIS) curves of a storage mode of supercapacitor (SC_{SM}) and an operating mode of supercapacitor (SC_{OM}). Resistance of the SCs under ambient temperature of RT was 161 kΩ and (b) dramatically decreased up to 3 Ω with phase transition of the ionogel at 45 ℃

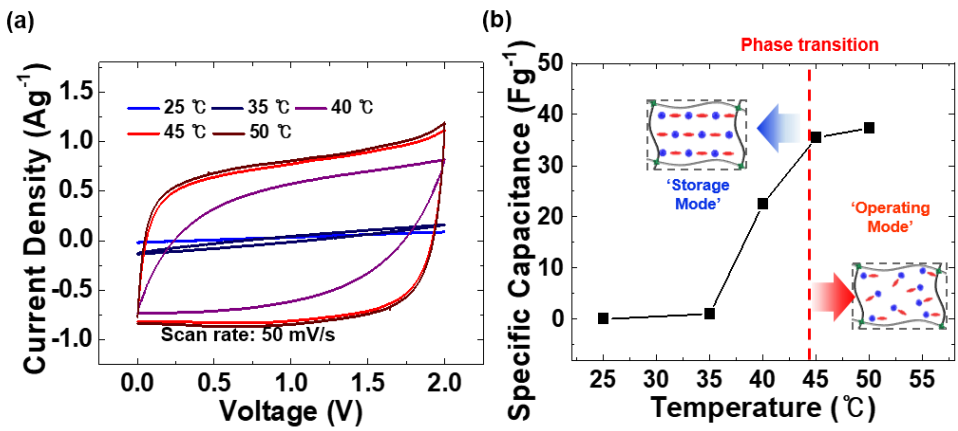

Figure 2.10 Electrochemical performance of ionogel electrolyte based supercapacitor. (a) Cyclic voltammetry (CV) curves of SCs under ambient temperature from 25 ℃ to 50 ℃. (b) Specific capacitance of a supercapacitor at different temperatures. The operating mode and storage mode was separated by the phase transition.

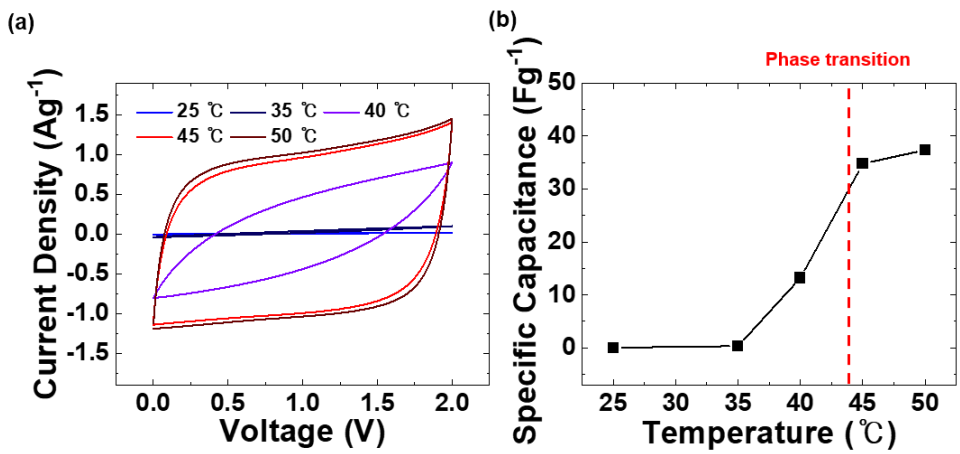

Figure 2.11 Electrochemical performance of pure ionic liquid electrolyte based supercapacitor. (a) Cyclic voltammetry (CV) curves of supercapacitor under temperature from 25 ℃ to 50 ℃. (b) Specific capacitance of a supercapacitor at different temperatures

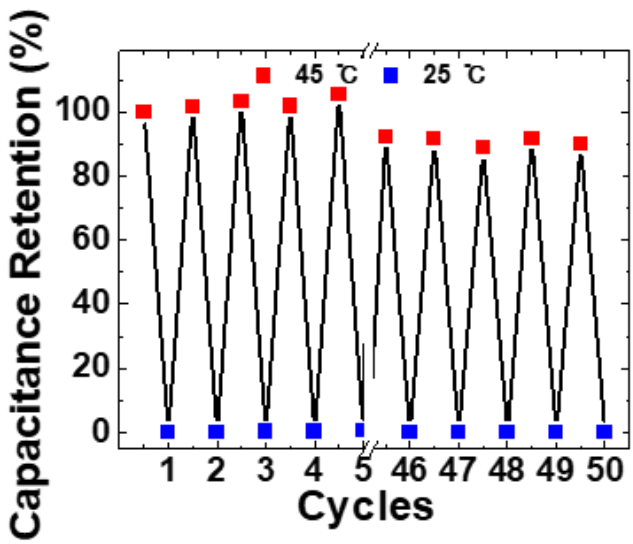

Figure 2.12 Reversibility of capacitance according to the temperature cycles; Red dot: 45 ℃, blue dot: 25 ℃.

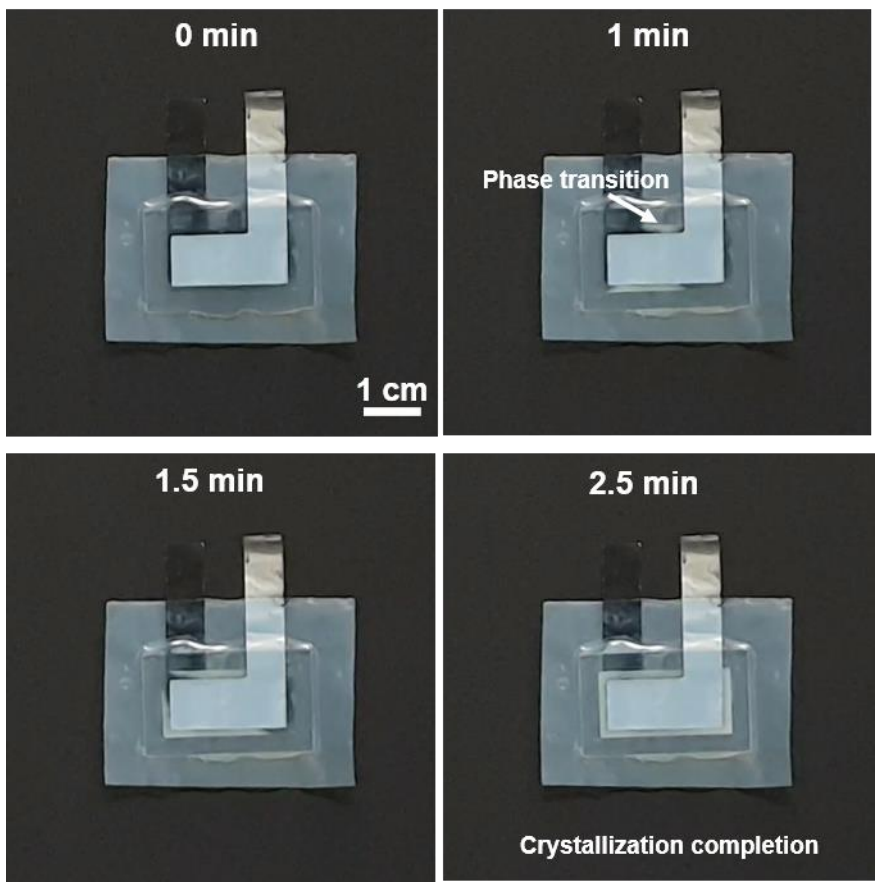

Figure 2.13 Real-time phase transition of SC. After lowering the temperature from 45 ℃ to 25 ℃, the phase transition started after 1 min and crystallization was completed after 2.5 min.

2.3.3 The capacitive performance of SCs in operating mode.

To measure the capacitive performance of SC, SC_{OM} was evaluated at 45 °C. At this point, the SC was fully operational in the two-electrode configuration. Figure 2.14a shows the CV measurements between 0 and 2 V at various scan rates from 5 to 200 mV s^{-1}. The rectangular shape of the CV curves at all scan rates indicates good capacitive behavior[34]. At a high scan rate of 200 mV s^{-1}, the rectangular shape of the CV curve is slightly distorted because there is insufficient time for interactions between the electrode and electrolyte[35]. The capacitive performance at different current densities was further confirmed by the GCD curves (Figure 2.14b). All GCD curves maintain a nearly symmetrical triangular shape at different current densities (0.2, 0.5, 1, 2, and 4 A g^{-1}) in the potential window of 0 – 2 V, indicating a high degree of reversibility in the charge/discharge process[36]. Based on the GCD measurements, the specific capacitance was calculated according to the current density (Figure 2.14c). The specific capacitance derived from GCD tests using a two-electrode system is determined by eqn (4); where C_m (F g^{-1}) is the specific capacitance, m is the total active materials mass of two electrode, Δt is the discharge time, I is the discharge current and ΔV is the working voltage window.

$$C_m = \frac{I\Delta t}{m\Delta V} \tag{4}$$

When the current density was 0.2 A g^{-1}, the capacitance was 25.2 F g^{-1}, and the capacitance gradually decreased as the current density increased. Figure 2.15a reveals the relationship between the energy density and power density of the SCs

(Ragone plot). The specific energy density (E, Wh kg^{-1}) and specific power density (P, W kg^{-1}) derived from GCD tests can be determined by eqn (5) and eqn (6); where C_m is the specific capacitance, ΔV is the potential window and Δt is the discharge time[37].

$$E = \frac{1}{2 \times 3.6} C_m \Delta V^2 \tag{5}$$

$$P = \frac{\mathrm{E}}{\Delta t} \times 3600 \tag{6}$$

The SC_{OM} exhibited an energy density of 7.77 Wh kg^{-1} at a power density of 4000 W kg^{-1}. The energy density and power density in this work are comparable to the performance of previously reported carbon electrode and ionic liquid such as $[Emim]^+[OAc]^-$[38], $[C_4mim]^+[OAc]^-$[39], $[Emim]^+[Cl]^-$[40], $[EMIH]^+[SO_4]^-$[41], $[Pyr_{14}]^+[Br]^-$[42] and $[EMIM]^+[BF_4]^-$[43] based supercapacitors. The long-term cyclic stability of the SC_{OM} was also examined using the cyclic charge-discharge system at a current density of 0.5 A s^{-1}, as shown in Figure 2.15b. The capacitance retention reached 87.5% after 3000 cycles, suggesting good electrochemical stability. Figure 2.16 shows the curves of SC_{OM} at different folding angles (pristine, 45°, 90°, 135° and 0°). The shapes of the CV curve show a negligible amount of change under all folding angles, indicating that the capacitive property of the SCs is not significantly affected by folding stress[44]. This is due to the flexibility of the ionogel. In addition, since the electrode and electrolyte are combined into one entity through in-situ polymerization, there is no deviation even when folded.

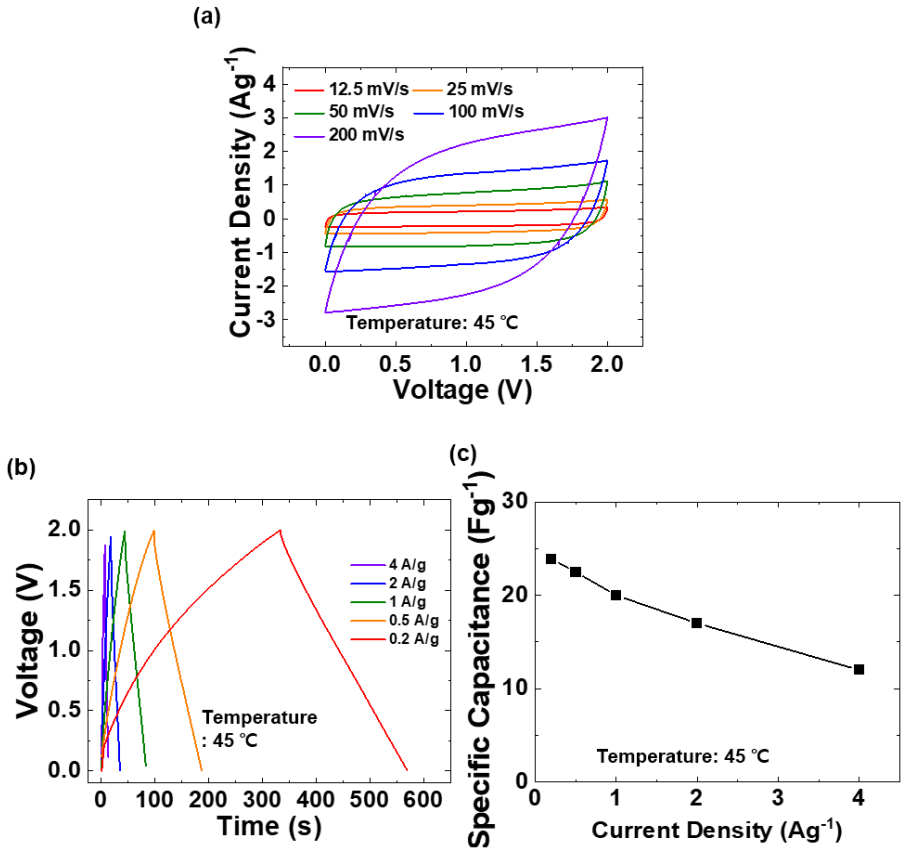

Figure 2.14 Electrochemical performance of phase-transitional SCs in operating mode. (a) Cyclic voltammetry curves of SC_{OM} at different scan rates from 12.5 to 200 mV s^{-1}. (b) Galvanostatic charge/discharge curves and (c) specific capacitance at current densities of 0.2, 0.5, 1, 2, 4 A g^{-1}

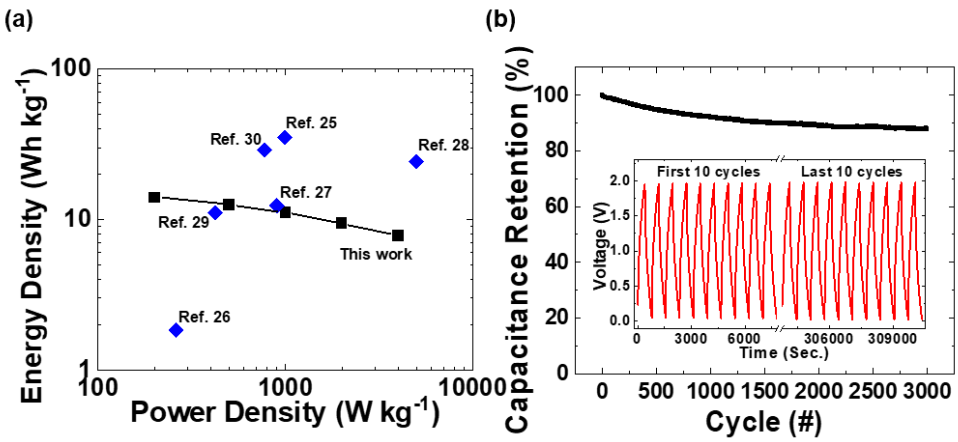

Figure 2.15 (a) A Ragone plot of the power density versus energy density for SC_{OM}. (b) Cyclic stability of SC_{OM} under applied current density of 0.5 A g^{-1}. Inset is charge-discharge cycles at first ten and final ten stages.

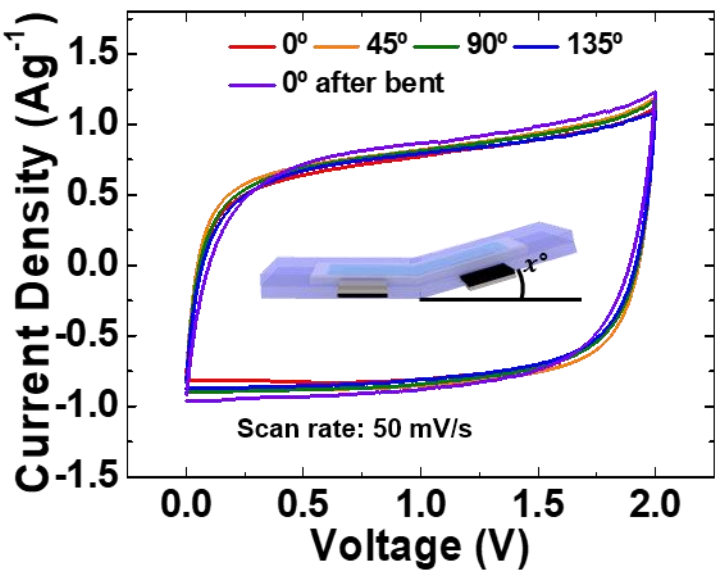

Figure 2.16 Cyclic voltammetry curves of SC_{OM} under bending deformation. Softness of the SCs and robust interface of electrode/ionogel led stable electrochemical performance.

2.3.4 Self-discharge characteristic of SCs in storage mode.

We have explored SC_{SM} that can suppress the movement of ions to reduce the self-discharge, which is a main drawback of SCs[45]. There are three mechanisms that describe the self-discharge; ohmic leakage, diffusion-controlled faradaic process and activation-controlled faradaic process[46, 47]. Among them, the diffusion-controlled faradaic process acted as the main self-discharge factor in our SCs. The diffusion-controlled model is expressed by eqn (7) where m is the diffusion parameter, the diffusion rate of the ions near the electrode surface[48].

$$V = V_o - m\sqrt{t} \tag{7}$$

Diffusion-controlled process is caused by the following mechanism. 1) Impurities such as Fe^{2+}/Fe^{3+} or O_2 create a shuttle effect[49]. Then, Faradaic reaction occurs by diffusion of depolarizing impurities into the electrode, causing charge leakage[50]. 2) During charging, the local ionic concentration at or near the carbon increases. After disconnection, some excess ions diffuse to an equilibrium state, reducing the charge in the carbon[47]. At room temperature, the ionogel electrolyte crystallizes to inhibit the diffusion of impurities and excess ions. Therefore, the self-discharge of SC_{SM} can be sufficiently suppressed. Figure 2.17 shows a schematic illustration of ion diffusion in SC_{OM} and SC_{SM}. After discharging, since excess ions and impurities can move easily in SC_{OM}, diffusion occurs. Therefore, charges are reduced by faradic reaction by cation impurities at the electrode and diffusion of excess ions. On the other hand, ions are crystallized and much less diffusion occurs in SC_{SM}. Therefore, after charging at a high temperature, a supercapacitor is capable of storing

charge for a long time in room temperature. To verify the effect of phase transition on self-discharge, the SCs were charged to 1.85 V with a current density of 0.02 A g^{-1} and held at this terminal voltage for 2 h at 45 ℃. Under the same conditions, the GCD curve was derived and it was measured that the energy density value as 22.71 Wh kg^{-1} (Figure 2.18). Then self-discharge was measured in two cases, SC_{SM} at room temperature and SC_{OM} at 45 ℃, through open circuit voltage (OCV) for 24 hours (Figure 2.19). In order to minimize the activation-controlled faradaic process, self-discharge caused by overcharging[51], the voltage was set to 1.85 V based on the stability window shown in the CV curve. According to the OCV curves, 57.79% of the initial voltage was maintained at 45 ℃ after 24 hours, while 89.51% was maintained at room temperature. This observation points to the outstanding performance over the existing ionic liquid-based SCs (Table 2.1). Figure 2.20a shows a fitted graph to which the diffusion-controlled model is applied. The self-discharge curve has a linear relationship between V and $t^{1/2}$, and the correlation coefficient R^2 is more than 0.99. Furthermore, the diffusion parameter m is 7.16×10^{-4} V $s^{-1/2}$, much lower than that of the conventional SCs ($3 \times 10^{-3} \sim 19 \times 10^{-3}$ V $s^{-1/2}$)[47]. This result indicates that the crystallized ionogel electrolyte effectively inhibits the movement of ions and impurities. As a result, self-discharge by diffusion was effectively suppressed. We represent the effect of ohmic leakage through a fitted graph (Figure 20b,c). Given that the graph is poor fit, it is concluded that ohmic leakage is also not a major factor. In order to demonstrate the practical usability of the synthesized SCs, they were connected to LED lights (Figure 21a). Each SC was charged to 2 V for 2 hours at 45 ℃ and then crystallized by lowering the temperature to room temperature.

Photographs of the green LED at each time point are presented in Figure 21b, and the DC light power of green LED output over time is plotted in Figure 21c. The LED light remained on for more than 3 hours. Since self-discharge was minimized by controlling the ionic conductivity of the SCs, most of the charging voltage could be used to turn on the LED.

Table 2.1 Self-discharge performance of ionic liquid-based SCs.

Ionic liquid	Charging voltage [V]	Discharging time [hours]	Self-discharge rate [%]	Ref.
$[EMIM]^+[Ac]^-$	1.5	3	20	[52]
$[BMIM]^+[Br]^-$	1.8	5	34.4	[53]
$[TEMA]^+[BF_4]^-$	2	24	29	[22]
$[EMIM]^+[BF_4]^-$	3	60	28.9	[48]
$[EMIM]^+[NO_3]^-$	1.85	24	10.49	This work

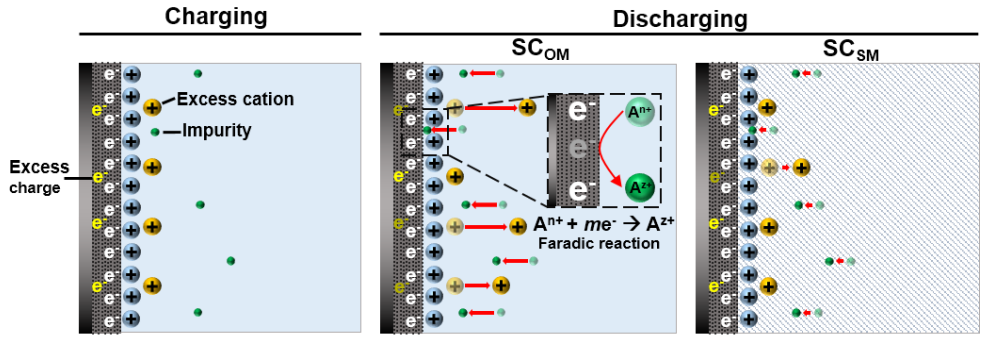

Figure 2.17 Schematic illustrations of charging and self-discharging processes of SC_{SM} and SC_{OM}. Self-discharge was described with a diffusion-controlled model.

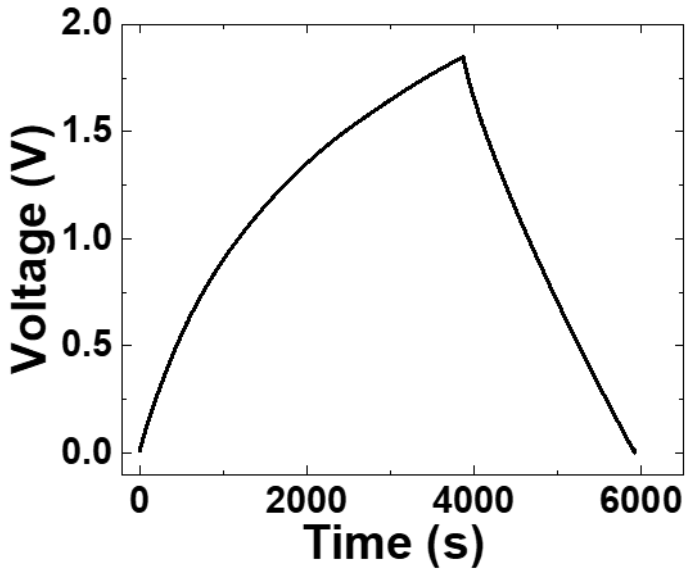

Figure 2.18 Galvanostatic charge/discharge (GCD) curves at current density of 0.02 A g^{-1}.

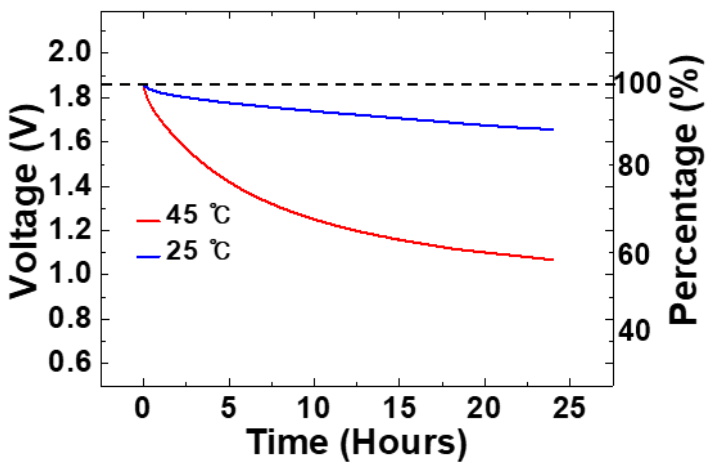

Figure 2.19 Self-discharging curves of a SC at 45 ℃ and 25 ℃. (c) A self-discharging curve of a supercapacitor at 25 ℃. The curve is fitted by the diffusion-controlled model. The measured diffusion parameter m is 7.16×10^{-4} V $s^{-1/2}$.

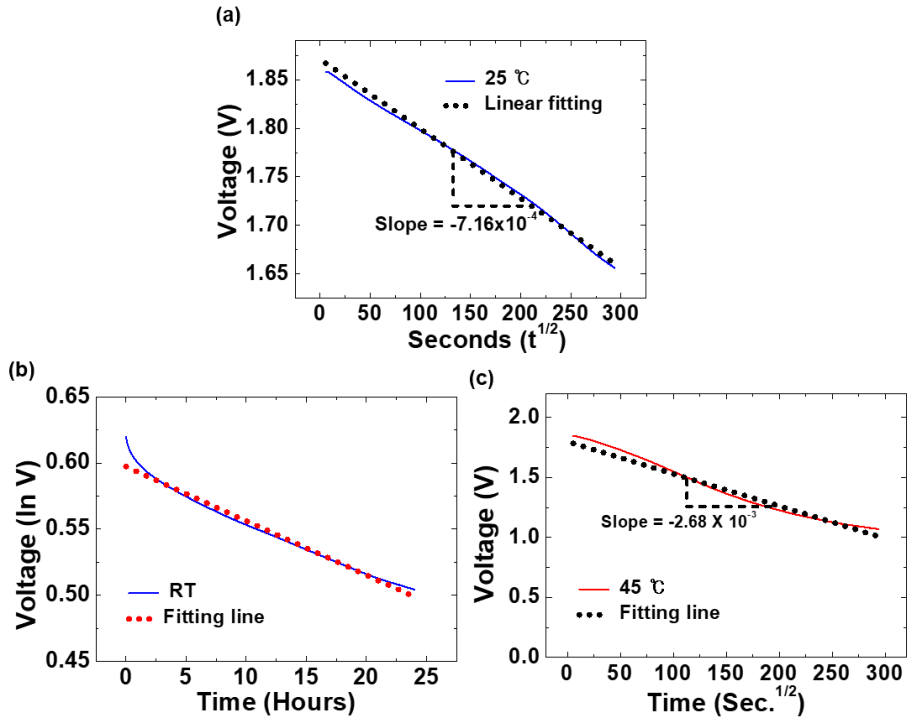

Figure 2.20 (a) A self-discharging curve of a supercapacitor at 25 ℃. The curve is fitted by the diffusion-controlled model. The measured diffusion parameter m is 7.16×10^{-4} V $s^{-1/2}$. (b) A self-discharging curve of a supercapacitor at room temperature (25 ℃) fitted by a ohmic leakage model. (c) A self-discharging curve of a supercapacitor at 45 ℃ fitted by a diffusion-controlled model. The measured diffusion parameter m is 2.68×10^{-3} V $s^{-1/2}$.

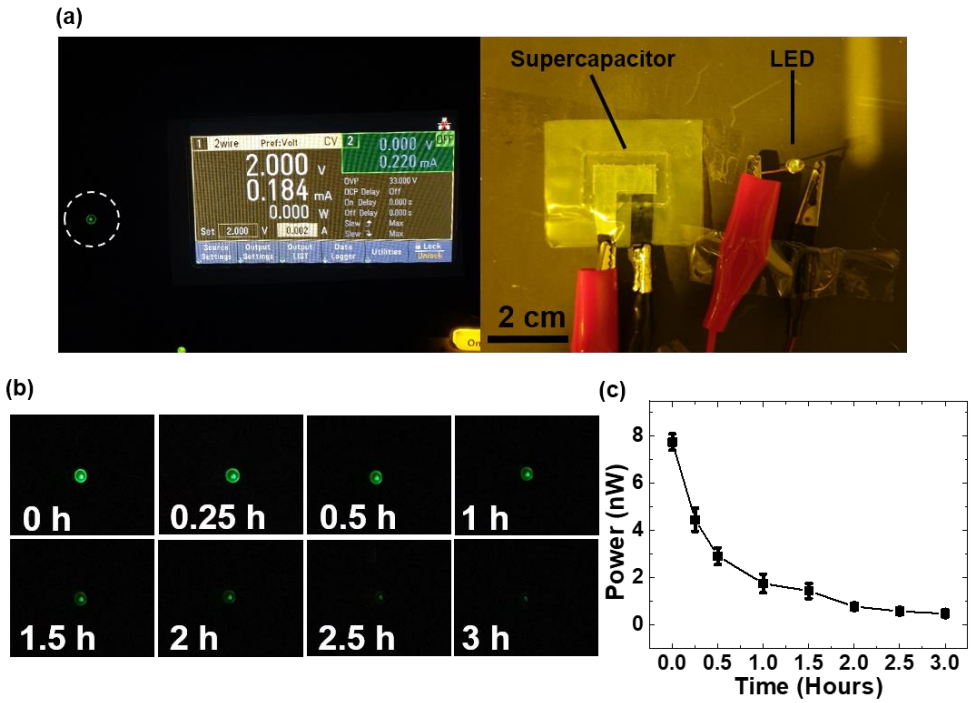

Figure 2.21 (a) LED is operated at a current of 100 ~ 200 μA and a voltage of 2 V by a DC power supply (KEYSIGHT, E36233A) and LED operation by a charged $SC_{SM.}$ (b, c) Suppressed self-discharging of the SC enhances optical power duration of a green LED during a discharging process.

2.4 Conclusion

In this study, we presented a supercapacitor based on a phase-transitional ionogel electrolyte for a selective operating/storage mode. To overcome various disadvantages of ionic liquid electrolytes such as leakage, corrosion and packaging problems, a phase-transitional ionic liquid and a polymer were combined using a photoinitiator to fabricate the ionogel electrolyte. In the ionogel manufacturing process, the bonding strength between the electrode and the electrolyte was improved through in-situ polymerization. By controlling the phase with a change in temperature, the ionogel can be made to be rigid and opaque below the melting point, where as it is flexible and transparent above the melting point. The EIS data shows a dramatic difference in resistance depending on the phase, indicating the effective control of ionic conduction. We investigated how the performance of the SCs changes with temperature. The results of the CV test confirmed that the phase-transitional SCs are activated/deactivated and show significant differences in capacitance with changes in temperature. To evaluate the capacitive performance of the SCs, CV and GCD tests were performed above the melting point in the operating mode. The SC_{OM} showed good capacitive behavior, high reversibility, stability and flexibility. In the storage mode, it was shown that self-discharge was significantly suppressed through a diffusion-controlled model. Therefore, it was confirmed that the LED device was turned on for a long time. We expect that phase-transitional SCs provide a better development and understanding of an energy storage device in the future.

Chapter 3. The Enhancement of Ionic Thermoelectric Seebeck Coefficient by Phase Difference

3.1 Introduction

Since the emergence of the 'Internet of Things (IoT)' concept, which integrates many things and surrounding things into a network, the IoT market is growing faster than ever before.[54]. At the same time, the growing demand for wireless sensor networks to connect objects increases the need for sustainable energy supply. A sustainable energy is mainly generated through the surrounding environment such as piezoelectric[55], triboelectric[56] and thermoelectric effect. Among themThe thermoelectric effect is an attractive method for regenerative energy conversion that generates dislocations in temperature gradients. Moreover, the thermoelectric effect is evaluated as an eco-friendly energy that utilizes generated body heat or waste heat energy. The thermoelectric effect is characterized by the Seebeck coefficient, which is defined as the potential generated under temperature gradient[57]. Conventional thermoelectric materials are based on bismuth or sulfide alloys, which exhibit the electronic thermoelectric effect. The Seebeck coefficients of the electronic thermoelectric materials have been reported to be ~μV/K[58]. However, conventional thermoelectric materials have limitations to be used in practical applications due to insufficient Seebeck coefficient to operate devices.

An ionic thermoelectric effect, on the other hand, is generated by the entropy carried by the ions[59]. The ionic thermoelectric effect shows a much higher Seebeck coefficient compared with electronic thermoelectric effect[60]. The thermogalvanic effect, one of the ionic thermoelectric mechanisms, harvests the reaction entropy of the ionic redox couple by maintaining the two electrodes at different temperatures[61]. However, the thermal power is still insufficient to be applied to wireless devices. Therefore, there have been efforts to increase the thermopower efficiency of thermogalvanic cells in various ways. For example, Yu, Boyang, et al. achieved a high Seebeck coefficient of 3.73 mV/K by adding guanidinium cations[62]. The guanidinium cations induced crystallization and dissolution of redox ions according to temperature. As a result, the Seebeck coefficient was increased by forming a larger and persistent ion concentration gradient. In addition, Duan, Jiangjiang, et al. used a thermo-sensitive nanogels to convert the Seebeck coefficient of thermogalvanic cell from 0.71 mV/K to -1.91 mV/K[63]. They showed that the nanogels selectively trap redox ions depending on temperature, causing p-n inversion, and improving thermoelectricity by connecting the two types in series. However, since the thermogalvanic effect still has limited methods to increase thermopower performance, it is necessary to introduce a new mechanism to improve the thermopower.

Here, we introduce the novel mechanism that presents the enhancement of the ionic thermoelectric effect induced by phase difference between low and high temperature region. A phase transition is a method that dramatically changes the flow of ion with temperature[24]. Beyond the effect of the temperature gradient, the large difference

in ion mobility due to the phase difference increases the difference in the interaction between the electrode and the ion at two temperatures, maximizing the thermoelectric effect. One of the ionic materials that can undergo a phase transition at ambient temperature is an ionic liquid[64]. Some ionic liquids have a melting point at ambient temperature, and are characterized by high thermal and electrochemical stability, high ionic conductivity and very low vapor pressure[12], making them suitable for ionic thermoelectric cell. The thermogalvanic cell was manufactured with silver/silver chloride (Ag/AgCl) electrode as the electrode and phase-transitional IL, 1-Allyl-3-methylimidazolium chloride ($[AMIM]^+[Cl]^-$), as the electrolyte. The fabricated thermogalvanic cell with phase difference, the liquid state at high temperature region and state solid state at low temperature region, showed enhanced the Seebeck coefficient compared to the thermogalvanic cell with uniform phase state.

3.2 Experimental section

3.2.1 Fabrication of the thermogalvanic cell

Silver/Silver chloride (Ag/AgCl) electrodes are fabricated by immersing Ag electrodes with a diameter of 0.5 mm in bleach and storing them in a saturated sodium chloride (KCl) solution at 40 ℃. A cell was manufactured by attaching an acrylic plate mold to a quartz plate bottom substrate with a size of 60 X 10 X 1 mm. For the preparation of the thermaogalvanic cell, electrodes were inserted into both

ends of the empty cell and melted $[AMIM]^+[Cl]^-$ electrolyte was added. After preparation, the temperature was lowered below the melting point to solidify the electrolyte.

3.2.2 Ionic liquid analysis

Differential scanning calorimetry (DSC) was performed using a TA Instruments Discovery DSC. The samples were analyzed over a temperature range of -20 ℃ to 100 ℃ with a heating rate of 2 ℃/min. The transmittance of crystallized and decrystallized ionic liquid at 30 ℃ and 60 ℃ were measured using UV-VIS spectroscopy (Agilent Technologies, Cary 60) over a wavelength range of 300 to 800 nm. X-ray diffraction (XRD) patterns (BRUKER, D8-Advance) of $[AMIM]^+[Cl]^-$ ionic liquid were obtained at 30 ℃ and 60 ℃ over an angular range of 10 to 60° with a step size of 0.6°.

3.2.3 Characterization of thermogalvanic cell thermoelectrical properties

The thermoelectric performance of the thermogalvanic cell was evaluated by applying different temperatures to both ends of the cell. The output voltage of the thermogalvanic cell was measured using a electrometer (KEITHLEY, 6517B) at several temperatures between the two plates. Electrochemical impedance spectroscopy (EIS) was performed using a potentiostat/galvanostat (Gamry Reference 600+) in

the frequency range of 0.1 Hz – 1 MHz. For EIS measurement, a cell using a platinum plate as an electrode was fabricated in a size of 15 × 10 × 2 mm.

3.3 Results and Discussion

3.3.1 A thermoelectric enhancement mechanism induced by phase difference

In this study, the effect of the phase difference on the improvement of the ionic thermoelectric effect was confirmed. The thermogalvanic system generates an electric potential by the redox reaction of the electrolyte according to the temperature gradient. In general, two types of compounds ($Fe(CN)_6^{3-}$, $Fe(CN)_6^{4-}$)[9, 65] or other redox pairs[66, 67] are widely used as electrolytes participating in redox reactions in thermogalvanic cells. 1-Allyl-3-methlyimidazolium chloride ($[AMIM]^+[Cl]^-$), an imidazolium-based ionic liquid, was used as the electrolyte for the thermoelectric cell since the $[AMIM]^+[Cl]^-$ have a moderate melting point (~ 50 °C). In addition, homemade Ag/AgCl electrodes were used to induce the electrochemical reactions with the chloride ions. The main driving force for generating the potential from the temperature difference is the tendency to balance the degree of interaction between the electrode and electrolyte in the low and high temperature regions. In conventional thermogalvanic cells that have a homogeneous liquid phase in the low and high regions, the chloride ions in the high temperature regions have higher active mobility than the chloride ions in the low temperature regions (Figure 3.1). Since the chloride

ions in the high temperature regions actively interact with the electrode, the oxidation reaction, $Ag+Cl^-(l) \rightarrow AgCl(s) + e^-$, occurs, and chloride ions near the electrode decrease. On the other hand, the reduction reaction of $AgCl(s) + e^- \rightarrow Ag + Cl^- (l)$ occurs near the electrode in the low-temperature region, increasing the number of chloride ions. In redox reactions, potentials are generated through the electron transfer. On the other hand, the thermoelectric effect is enhanced since the interaction between the electrode and electrolyte is significantly different in the low and high temperature regions in the phase different thermogalvanic cell (Figure 3.2). The ionic liquid in the high-temperature region interacts with an electrode like a conventional thermoelectric cell to cause an oxidation reaction ($Ag + Cl^-(l) \rightarrow AgCl(s) + e^-$), but the interaction between the electrode in the low-temperature region and the chloride ions is much less. This is a result of the chloride ion being fixed in the lattice structure of the crystallized ionic liquid, and the mobility is greatly reduced compared to the mobility in the liquid phase at the same temperature. Thus, a relatively improved driving force is generated to balance the interaction between the electrolyte and the electrode in the cold and hot regions. As a result, the mobility difference of ions due to the phase difference creates a synergistic effect with the mobility difference from the temperature difference to generate a huge potential.

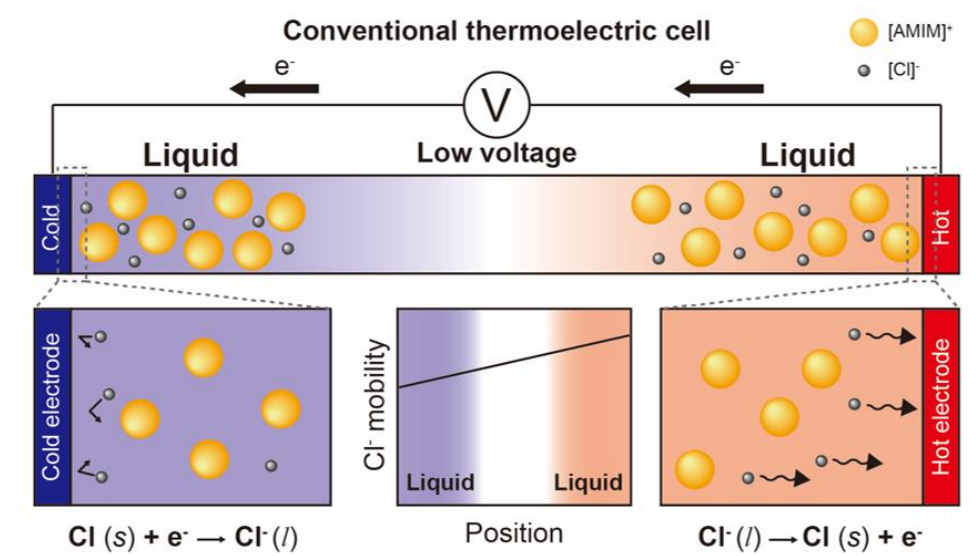

Figure 3.1 In conventional thermoelectric cells, when a temperature difference occurs between electrodes, an electric potential is generated through redox reaction of chloride ions. The mobility of Cl- anions steadily increases with increasing temperature.

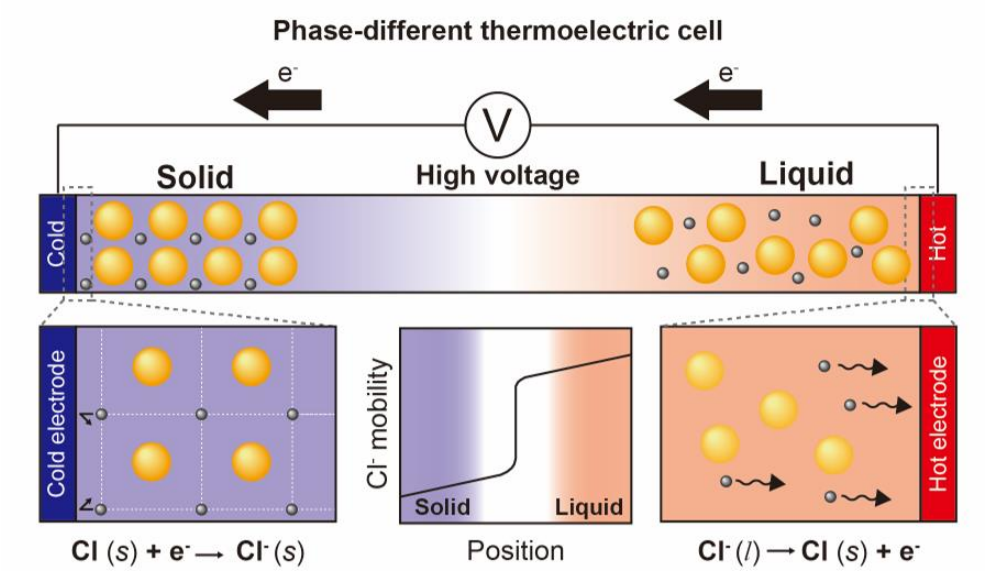

Figure 3.2 Different-phase thermoelectric cells result in higher potentials due to the increased mobility of chloride ions induced by the different phases between the low and high temperature electrodes. In the solid phase, chloride ion movement is inhibited by the lattice structure, whereas in the liquid ion movement is free. As the phase changes from solid to liquid, the mobility of chloride ions increases rapidly. As a result, there is a large difference in the interaction between the chloride ions and the electrode at both temperatures, which enhances the thermoelectric effect.

3.3.2 Properties of the ionic liquid in different phases.

The phase transitional behavior of $[AMIM]^+[Cl]^-$ ionic liquid electrolyte for a thermogalvanic cell is optically shown in Figure 3.3a. A phase-transitional ionic liquid is known to form a crystal lattice below the melting point[24]. When the temperature of the bottom of the phase transitional ionic liquid, $[AMIM]^+[Cl]^-$, contained in the vial was raised to 60 ℃, a definite phase difference was confirmed. The optical microscopic pictures showed that the crystal lattice structures were observed as the ionic liquid in a crystallized state at 30 ℃, while a homogenous liquid state was observed as the ionic liquid was decrystallized at 60 ℃. Figure 3.3b shows a chemical structure of the $[AMIM]^+[Cl]^-$ crystal. It was reported that the $[AMIM]^+[Cl]^-$ has crystal structure with space group P21/c (a= 7.931, b=12.836, c=16.452 Å, β= 96.22°)[68]. DSC measurements were carried out to investigate the phase transition temperature of $[AMIM]^+[Cl]^-$ IL (Figure 3.4a). The DSC graph shows that the $[AMIM]^+[Cl]^-$ IL has the melting point of 53.1 ℃. In order to observe the transparency according to the phase transition in the visible light region, the transmittance of the IL was measured in the wavelength range of 300 to 800 nm using spectroscopy (Figure 3.4b). The transmittance spectra show that the transmittance of an decrystallized ionic liquid approaches 100% at a wavelength of 800 nm and then gradually decreases toward 300 nm at 60 ℃. Because the ionic liquid is a yellow transparent liquid, it shows a similar to the case of the transmittance curve of the yellow filter[69]. On the other hand, the transmittance of the crystallized ionic liquid at 30 ℃ in the entire wavelength rage has not been verified. Figure 3.4c shows the XRD patterns of

crystallized and decrystallized IL. IL at 30°C exhibits an XRD peak due to crystallinity, but IL at 60°C does not exhibit a peak. To determine the interaction of ions with electrodes at each phase, EIS measurement was conducted. In order to form an electrical double layer (EDL), a cell was fabricated using platinum electrodes and EIS was measured at 30 ℃ and 60 ℃ (Figure 3.5. Figure 3.6a,b show the nyquist plots of the cell at 30 and 60 ℃. The EIS plot represents a semicircle at high frequencies and an oblique line at low frequencies. The diameter of the semicircle is the sum of the electrolyte resistance and the electrode resistance[32], and resistivity of 69,970 and 432.13 Ω·cm were measured at 30 ℃ and 60 ℃, respectively. The values of diffusion coefficient (D) , mobility (μ) and number density of the charge carrier of ions (n) near the electrode were obtained by fitting the plot[70]. Table 3.1 shows the parameters derived by nyquist fitting. At 30 and 60 ℃, the diffusion coefficient and mobility of the ionic liquid were 6776 times and 6198 times different, respectively. Especially, the number density of the charge carrier of ions was calculated to be 38.1 times higher at 30 ℃ than at 60 ℃. This is because the density increased as the volume of ionic liquid decreased during crystallization at 30°C.

Table 3.1 The values of D, μ, n of $[AMIM]^+[Cl]^-$ IL based electrolyte.

Temperature	D ($\times 10^{-10}$ cm^2/s)	μ ($\times 10^{-9}$ $cm^2 \cdot s/V$)	N ($\times 10^{20}$ cm^{-3})
30 ℃	1.89	7.2	337.9
60 ℃	12807.2	44626.9	8.86

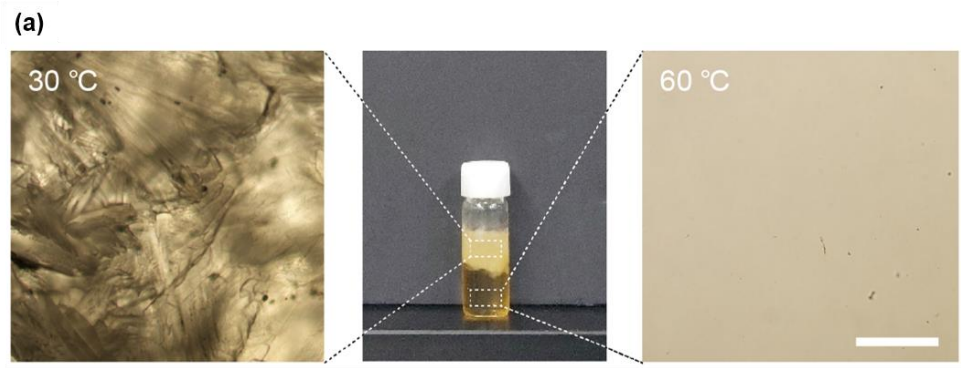

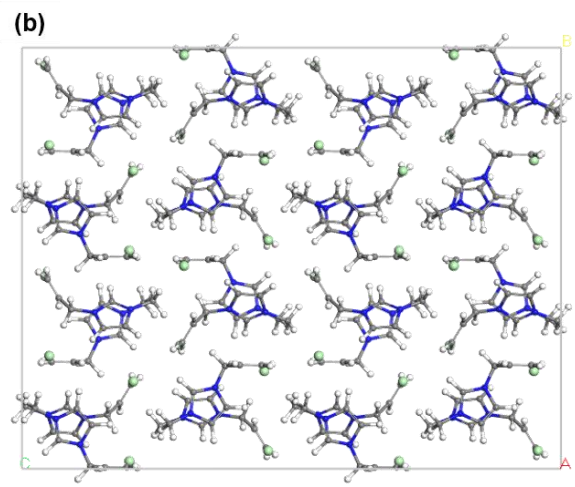

Figure 3.3 (a) Optical micrographs and picture of $[Amim]^+[Cl]^-$ at low and high temperaturesAt 30°C, the ionic liquid exists as a solid and the crystal structure is observed, but at 60°C, since the ionic liquid exists as a liquid, nothing is detected. Scale bar, 100 μm. (b) A chemical structure of the $[Amim]^+[Cl]^-$ crystal with space group P21/c (a= 7.931, b=12.836, c=16.452 Å, β= 96.22°)

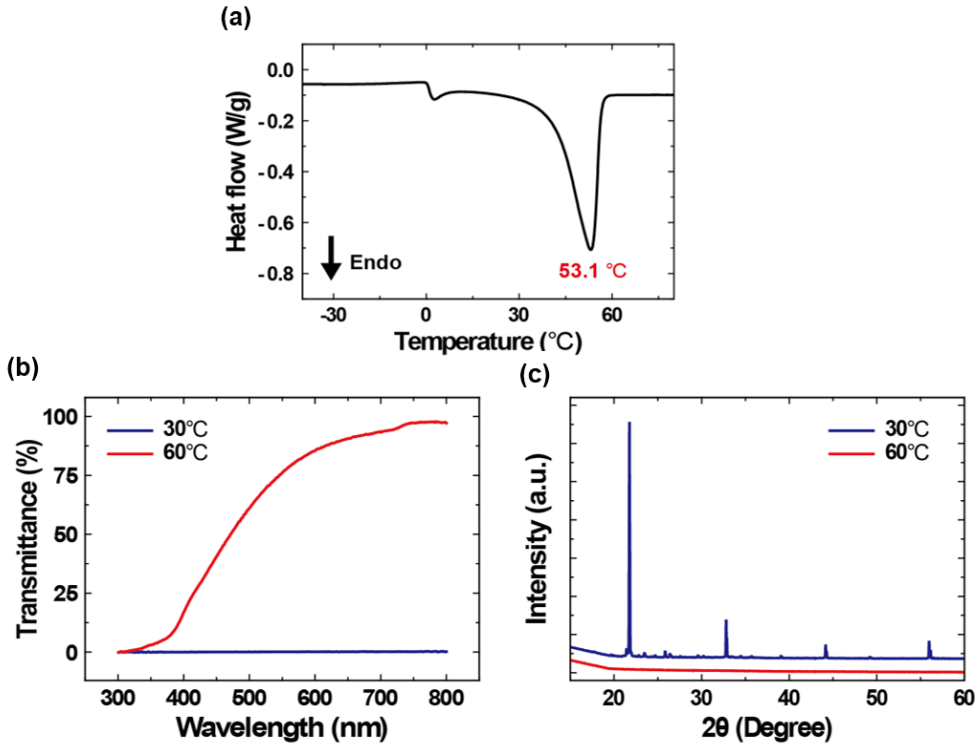

Figure 3.4 (a) DSC curve of the $[Amim]^+[Cl]^-$, heating from -50 to 80 ℃. The melting point of the $[Amim]^+[Cl]^-$ is shown as 53.1 ℃. (b) Transmittance of $[Amim]^+[Cl]^-$ in the visible light region with a wavelength of 300 to 800 nm at both temperatures. $[Amim]^+[Cl]^-$ ionic liquid showed no permeability at 30 ℃, while the ionic liquid shows similar permeability to that of the yellow filter at 60 ℃. (c) X-ray diffraction curve of the $[Amim]^+[Cl]^-$ ionic liquid at 30 and 60 ℃. The crystallized $[Amim]^+[Cl]^-$ shows the XRD peaks at 30 ℃ while the decrystallized $[Amim]^+[Cl]^-$ presents no XRD peaks at 60 ℃.

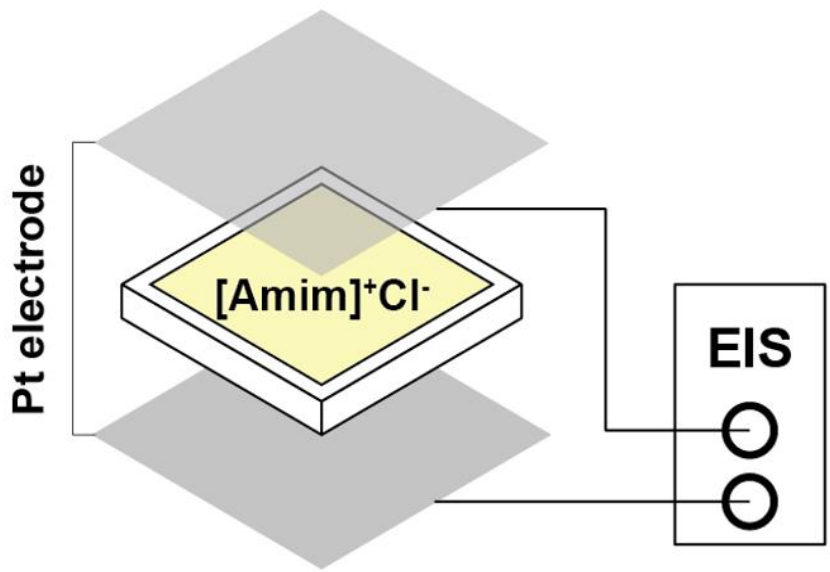

Figure 3.5 The schematic illustration of electrochemical impedance spectroscopy (EIS) measurements.

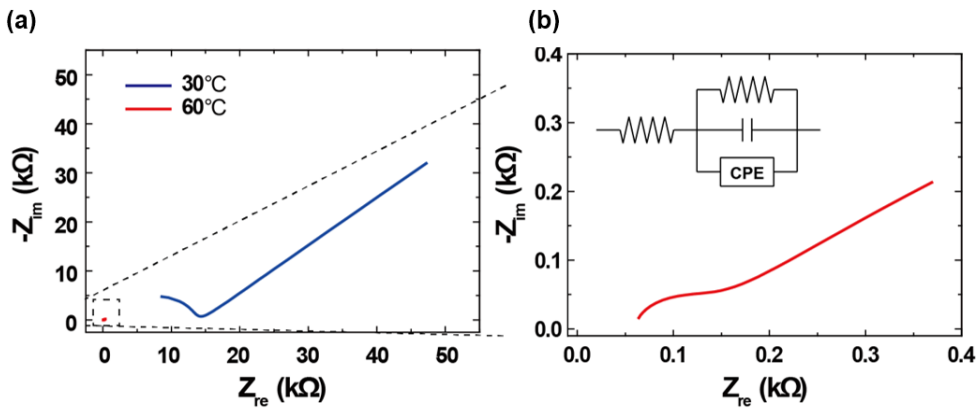

Figure 3.6 The nyquist plots of the thermoelectric cell at (a) 30 and (b) 60 ℃. The inset of the plot shows the equivalent circuit of EIS system.

3.3.3 Thermoelectric performance of $[Amim]^+[Cl]^-$ based thermogalvanic cell

We synthesized thermogalvanic cells based on the phase transitional ionic liquid electrolyte with Ag/AgCl electrodes. Figure 3.7 is schematic and picture of manufactured thermogalvanic cell. The cell was designed by attaching an acrylic plate mold to a quartz plate bottom substrate with high thermal conductivity. Then, the cell fabrication was completed by injecting molten ionic liquid and inserting handmade electrodes into both ends. It is confirmed that the IL electrolyte state is clearly distinguished according to the phase. To verify the effect of the phase difference on the Seebeeck coefficient, the Seebeck coefficients of the thermogalvanic cell with different phases were measured (Figure 3.8). Since an $[AMIM]^+[Cl]^-$ IL has a melting point of 53.1 ℃, the output voltages of thermogalvanic cells were measured by dividing the temperature into three sections according to the phases, solid – solid, solid – liquid and liquid – liquid. In a homogeneous stat, solid – solid state and liquid – liquid state, the Seebeck coefficients are 0.83 mV/K and 1.83 mV/K respectively. On the other hand, in the heterogeneous state, the solid – liquid state, the Seebeck coefficient obtained 3.33 mV/K. This result shows that the Seebeck coefficient increases as the difference in the interaction between ions and the electrode is maximized in different phases compared to the homogeneous state. Figure 3.9a shows power-voltage-current (*P-V-I*) characteristics of the phase different thermogalvanic cell. Using a variable resistor, the OCV was measured by changing the resistance from 100 MΩ to 200 Ω in each phase section. The fabricated thermogalvanic cell generated powers of 0.35 and 2.42 nW at 0 – 30 °C and 60 – 90 °C, respectively. As the temperature

changed to 30 – 60 °C, the power significantly increased to 11.8 nW, resulting in 33.7 and 4.8 times improvement in the power output by compared to the homogeneous state. Since the fabricated thermogalvanic cell is based on chloride ion and Ag/AgCl electrode, it could be used until the AgCl of one electrode is completely used. Therefore, the change of the output voltage was measured at 30 – 60 °C for a long period of time. As shown in Figure 3.9b, it was demonstrated that the OCV was stable for more than 50 hours. To evaluate the performance of thermogalvanic cells according to the length and connection in series, the Seebeck coefficients and OCVs were measured with increasing the cell length and number of cells. As shown in Figure 3.10a, the Seebeck coefficient changes were negligible with cell length. Additionally, the output voltage increased proportionally as the number of cell increased from 1 to 4 (Figure 3.10b). These results demonstrate the possibility of applying manufacturedThese results demonstrate the possibility of applying manufactured cells to devices requiring specific design and performance. cells to devices requiring specific design and performance.

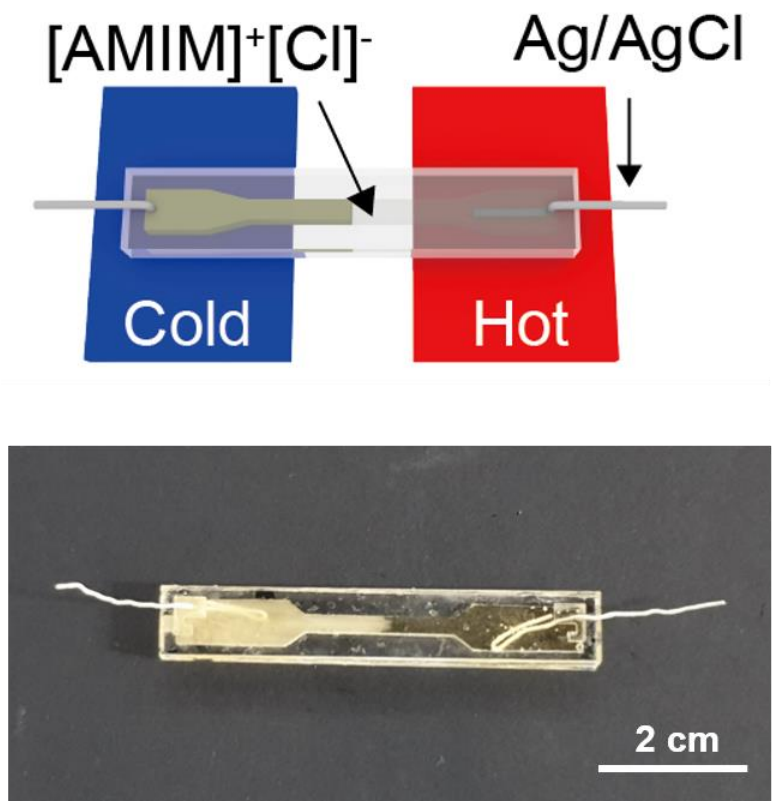

Figure 3.7 The schematic illustration and picture of thermogalvanic cell. A clearly distinct phase is observed depending on the temperature.

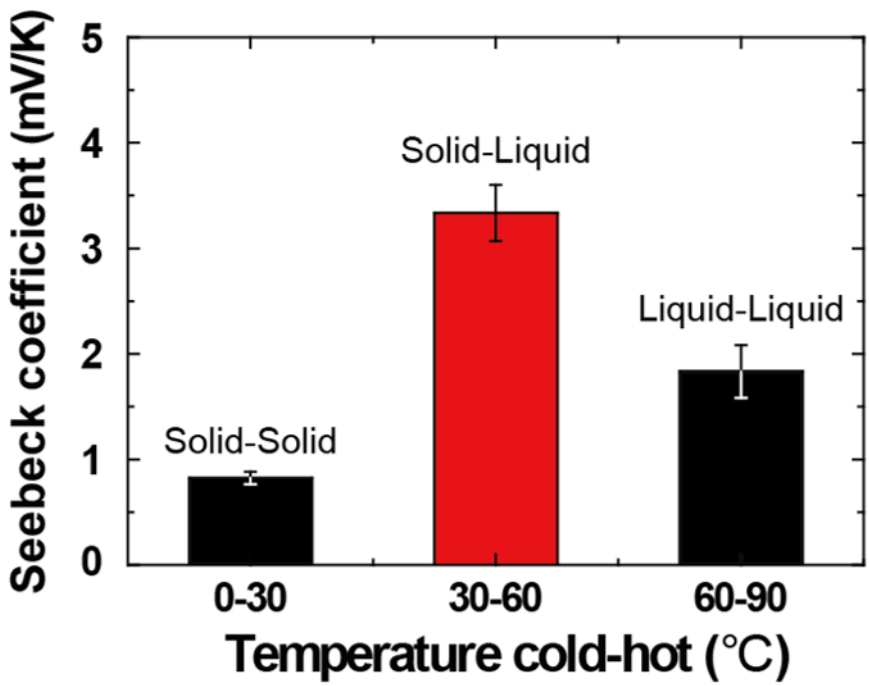

Figure 3.8 Seebeck coefficients of [Amim]+[Cl]- according to different phase states. The solid-solid and liquid-liquid phase thermogalvanic cells exhibit Seebeck coefficients of 0.83 and 1.83 mV/K, respectively, and the solid-liquid thermogalvanic cells exhibit improved Seebeck coefficients of 3.33 mV/K.

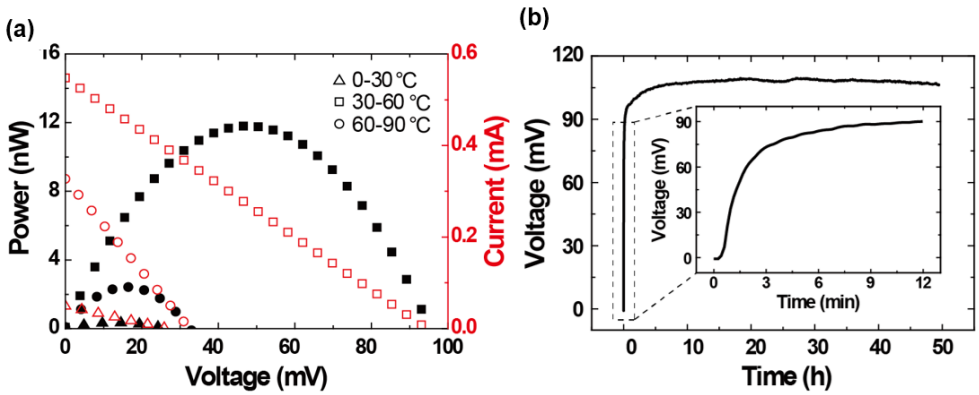

Figure 3.9 (a) Power-voltage-current (*P-V-I*) characteristics of thermogalvanic cell with different phase state. In the heterogeneous state, the maximum power is dramatically improved. (b) Stability of thermogalvanic cells over time. In the heterogeneous phase, the OCV was stable for more than 50 hours.

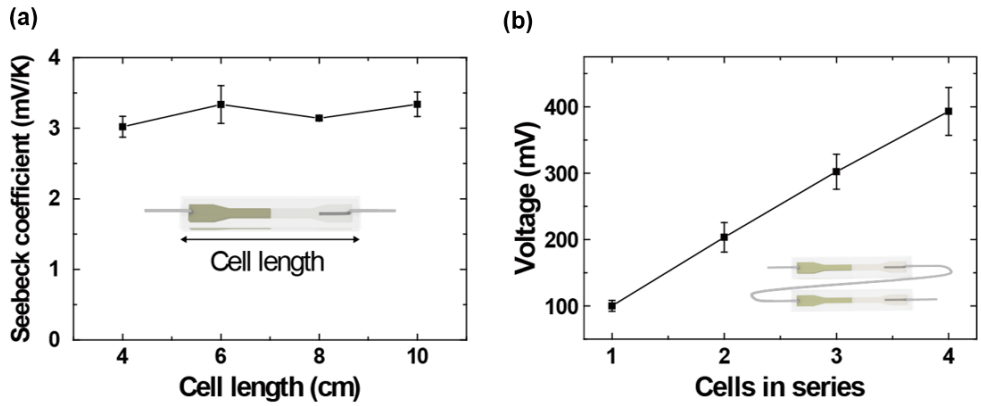

Figure 3.10 (a) Seebeck coefficient depending on cell length. The change of Seebeck coefficient with the change of cell length was insignificant. (b) Generation voltage of thermoelectric cells connected in series. The voltage increased proportionally to the number of cells.

3.3.4 Thermoelectric performance of other phase transitional ionic liquids.

We demonstrate the improvement of Seebeck coefficient by phase difference using $[AMIM]^+[Cl]^-$, a chloride-based ionic liquid with a melting point of 53.1 °C. In order to generalize the Seebeck coefficient enhancement by phase transition, other ionic liquids based on chloride ions were investigated. We chose 1-(2-hydroxyethyl)-3-methylimidazolium chloride ($[HOEtMIM]^+[Cl]^-$), 1-ethyl-3-methylimidazolium chloride ($[EMIM]^+[Cl]^-$) and tetrabutylammonium chloride (TBAC) as ILs with melting points of 83, 84, and 70 °C, respectively. Figure 3.12 shows the structural formulas of the phase-transitional ionic liquids. Then, thermogalvanic cells were manufactured by the previous method using each IL as electrolye, and the Seebeck coefficients were calculated for each phase (Figure 3.13). First, the output voltage of $[HOEtMIM]^+[Cl]^-$ were measured by dividing the phase state into three sections; solid – solid (40 – 70 ℃), solid – liquid (70 – 100 ℃) and liquid – liquid (100 – 130 ℃). The Seebeck coefficients measured 1.86 mV/K and 2.2 mV/K in the solid – solid state and the liquid – liquid state, and 2.76 mV/K in the solid – liquid state. Second, $[EMIM]^+[Cl]^-$ IL based cells were evaluated under the same conditions. The Seebeck coefficients were 1.86 and 2.06 mV/K in the homogeneous state, and 2.96 mV/K in the solid – liquid state. Finally, $[EMIM]^+[Cl]^-$ IL based cells were evaluated by dividing the phase into three sections; solid – solid (30 – 60 ℃), solid – liquid (60 – 90 ℃) and liquid – liquid (90 – 120 ℃). In each section, Seebeck coefficients of 1.67, 2.08 mV/K were measured in homogenous state and 3.8 mV/K were measured in solid – liquid state. Based on these results, we confirmed that the interactions

between chloride ions and electrodes at low and high temperatures were significantly different for all considered ILs in the heterogeneous phase state. Therefore, the thermoelectric effect has been greatly enhanced by distinguishing the phases of the cold and hot regions for all of the considered ILs.

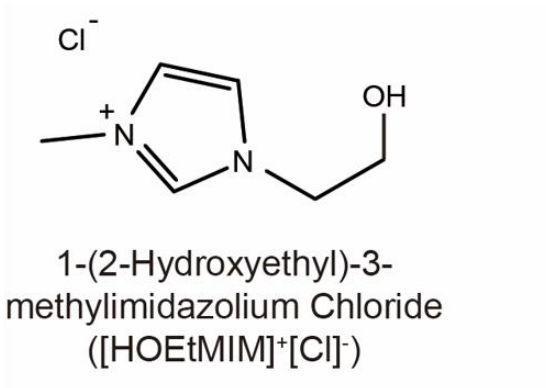

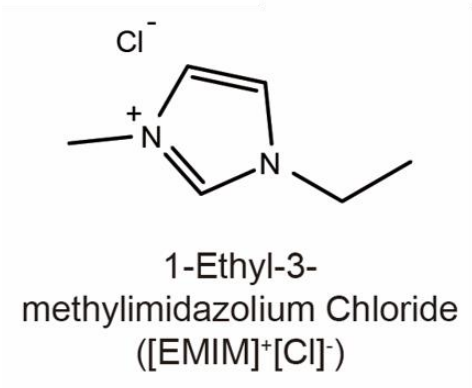

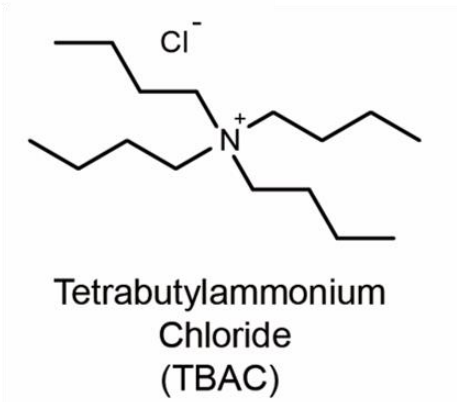

Figure 3.11 The chemical structures of the phase-transitional ionic liquid; $[HOEtMIM]^+[Cl]^-$, $[EMIM]^+[Cl]^-$ and TBAC.

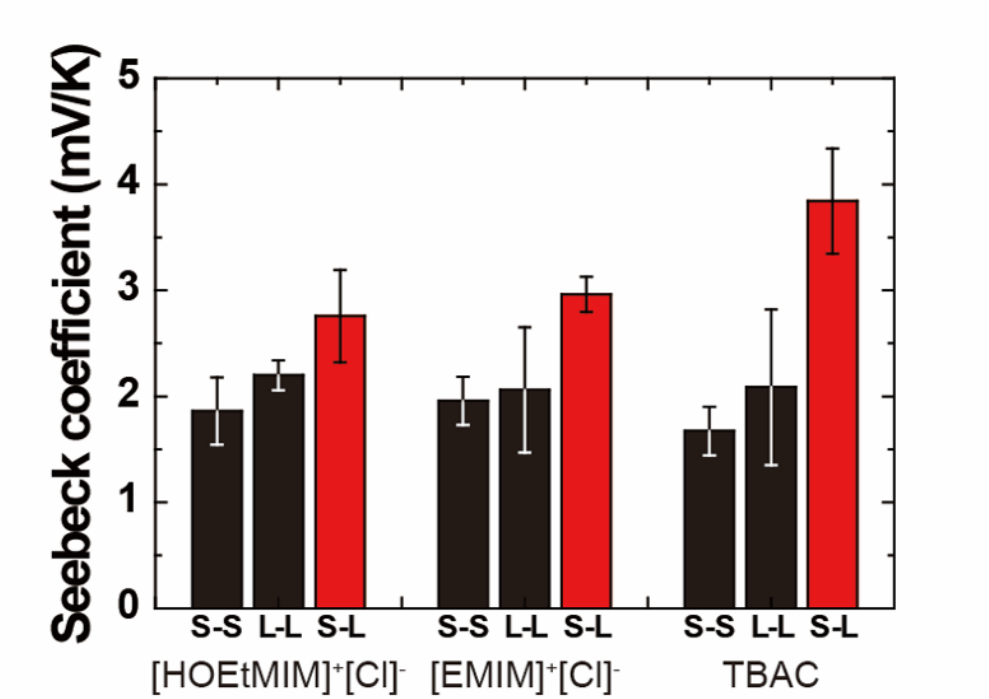

Figure 3.12 Seebeck coefficient of phase transition ionic liquids depending on temperature range. All ionic liquids exhibit improved Seebeck coefficients in a homogeneous state.

3.4 Conclusion

In previous studies, in order to maximize the difference in ion mobility between cations and anions, the ionic thermoelectric effect was strengthened mainly through chemical approaches, such as synthesizing composite materials or adding additives that synergistically induce the thermoelectric effect. Although the performance of the ionic thermogalvanic cell has been improved through previous studies, it is still insufficient to be put into practical use. Therefore, various mechanisms and methods need to be developed. In this study, we demonstrated a physical strategy that induces phase differences in low and high temperature areas to improve the ionic thermoelectric effect without additional components. We confirmed that the thermoelectric effect was enhanced when solid-liquid phase difference is present in the low and high temperature regions. Moreover, our method is effectively applied to all kinds of ionic liquids, greatly improving the thermoelectric effect. Therefore, this study shows that the thermoelectric effect of various ionic liquids can be strengthened by inducing phase differences. In particular, to the best of author's knowledge, this is the novel method to improve thermoelectric effect for ionic thermoelectric materials without any additives. Our strategy is expected to synergize with previous studies to dramatically improve the thermoelectric effect and ultimately accelerate the commercialization of thermogalvanic cells.

Chapter 4. Summary

In this thesis, phase-transitional ionic liquids are introduced into the energy supply system. Phase transition is a method to dramatically control the movement of ions with temperature. Therefore, it is possible to fabricate a device with a new function or an improved performance by applying it to a device whose operating mechanism is ion movement. The contents include (i) selectively operative supercapaccitors through phase transition and (ii) strategy to enhance the thermoelectric effect through novel mechanisms.

In the first part, I have fabricated a supercapactor using a phase transtional ionogel. By using the in-situ polymerization method, a physically and chemically stable and flexible supercapacitor was designed. The fabricated supercapacitor is operated only when the ionogel is activated above the melting point. I distinguish supercapacitors into the ‘Operating mode’ and ‘Storage mode’ according to phase. It is demonstrated that the specific capacitance of the active-inactive state changes dramatically, and the change of specific capacitance is repetitive. Morevoer, the performance of the supercapacitors in operating mode is evaluated. Finally, it is demonstrated to suppress the self-discharge, which is known as a main disadvantage of supercapacitors. I believe that the alternating mode of supercapacitors opens new possibilities for the development of supercapacitors as energy storage devices.

In the second part, I proposed a novel mechanism to increase the thermoelectric effect through phase transition. A thermogalvanic system based on chloride ions is

introduced using Ag/AgCl electrodes. Cells were fabricated using $[AMIM]^+[Cl]^-$ electrolyte, and Seebeck coefficients were evaluated in various temperature ranges. Through OCV measurement, it is verified that the Seebeck coefficient is changed according to the phase, and in particular, it is significantly enhanced in the solid-liquid phase. Moreover, I performed the same measurements for other phase transitional ionic liquids containing chloride ions. As a result, it is demonstrated that the Seebeck coefficient increases dramatically in all ionic liquids in the heterogeneous state. This study presents new possibility for research and method to enhance the thermoelectric effect, which are still in the early stages, and I believe that this mechanism is a strategy to accelerate the commercialization of thermoelectrics.

References

[1] J. Castro-Gutiérrez, A. Celzard, V. Fierro, Energy storage in supercapacitors: Focus on tannin-derived carbon electrodes, Frontiers in Materials 7 (2020) 217.

[2] J. Libich, J. Máca, J. Vondrák, O. Čech, M. Sedlaříková, Supercapacitors: Properties and applications, Journal of Energy Storage 17 (2018) 224-227.

[3] B. Hsia, M.S. Kim, C. Carraro, R. Maboudian, Cycling characteristics of high energy density, electrochemically activated porous-carbon supercapacitor electrodes in aqueous electrolytes, Journal of Materials Chemistry A 1(35) (2013) 10518-10523.

[4] R. Drummond, C. Huang, P. Grant, S. Duncan, Overcoming diffusion limitations in supercapacitors using layered electrodes, Journal of Power Sources 433 (2019) 126579.

[5] B. Pal, S. Yang, S. Ramesh, V. Thangadurai, R. Jose, Electrolyte selection for supercapacitive devices: A critical review, Nanoscale Advances 1(10) (2019) 3807-3835.

[6] M.A. Buckingham, F. Marken, L. Aldous, The thermoelectrochemistry of the aqueous iron (ii)/iron (iii) redox couple: significance of the anion and pH in thermogalvanic thermal-to-electrical energy conversion, Sustainable Energy & Fuels 2(12) (2018) 2717-2726.

[7] M.A. Buckingham, K. Laws, H. Li, Y. Kuang, L. Aldous, Thermogalvanic cells demonstrate inherent physiochemical limitations in redox-active electrolytes at water-in-salt concentrations, Cell Reports Physical Science 2(8) (2021) 100510.

[8] H. Wang, X. Zhuang, W. Xie, H. Jin, R. Liu, B. Yu, J. Duan, L. Huang, J. Zhou, Thermosensitive-CsI3-crystal-driven high-power I−/I3− thermocells, Cell Reports Physical Science (2022) 100737.

[9] J. Duan, G. Feng, B. Yu, J. Li, M. Chen, P. Yang, J. Feng, K. Liu, J. Zhou, Aqueous thermogalvanic cells with a high Seebeck coefficient for low-grade heat harvest, Nature communications 9(1) (2018) 1-8.

[10] C.-G. Han, X. Qian, Q. Li, B. Deng, Y. Zhu, Z. Han, W. Zhang, W. Wang, S.-P. Feng, G. Chen, Giant thermopower of ionic gelatin near room temperature, Science 368(6495) (2020) 1091-1098.

[11] Z. Lei, B. Chen, Y.-M. Koo, D.R. MacFarlane, Introduction: ionic liquids, Chemical Reviews 117(10) (2017) 6633-6635.

[12] J. Feng, Y. Wang, Y. Xu, Y. Sun, Y. Tang, X. Yan, Ion regulation of ionic liquid electrolytes for supercapacitors, Energy & Environmental Science 14(5) (2021) 2859-2882.

[13] A. Eftekhari, Supercapacitors utilising ionic liquids, Energy Storage Materials 9 (2017) 47-69.

[14] C.F. Francis, I.L. Kyratzis, A.S. Best, Lithium-ion battery separators for ionic-liquid electrolytes: a review, Advanced Materials 32(18) (2020) 1904205.

[15] Z.A. Akbar, Y.T. Malik, D.H. Kim, S. Cho, S.Y. Jang, J.W. Jeon, Self-Healable and Stretchable Ionic-Liquid-Based Thermoelectric Composites with High Ionic Seebeck Coefficient, Small (2022) 2106937.

[16] E. Frackowiak, F. Béguin, Supercapacitors: Materials, Systems and Applications, Poznan: Wiley-VCH Verlag GmbH & Co (2013).

[17] A. González, E. Goikolea, J.A. Barrena, R. Mysyk, Review on supercapacitors: Technologies and materials, Renewable and Sustainable Energy Reviews 58 (2016) 1189-1206.

[18] S. Banerjee, B. De, P. Sinha, J. Cherusseri, K.K. Kar, Applications of supercapacitors, Handbook of Nanocomposite Supercapacitor Materials I, Springer2020, pp. 341-350.

[19] J. Kowal, E. Avaroglu, F. Chamekh, A. Šenfelds, T. Thien, D. Wijaya, D.U. Sauer, Detailed analysis of the self-discharge of supercapacitors, Journal of Power Sources 196(1) (2011) 573-579.

[20] W. Zhang, W. Yang, H. Zhou, Z. Zhang, M. Zhao, Q. Liu, J. Yang, X. Lu, Self-discharge of supercapacitors based on carbon nanotubes with different diameters, Electrochimica Acta 357 (2020) 136855.

[21] H. Wang, Q. Zhou, B. Yao, H. Ma, M. Zhang, C. Li, G. Shi, Suppressing the Self-Discharge of Supercapacitors by Modifying Separators with an Ionic Polyelectrolyte, Advanced Materials Interfaces 5(10) (2018) 1701547.

[22] M. Xia, J. Nie, Z. Zhang, X. Lu, Z.L. Wang, Suppressing self-discharge of supercapacitors via electrorheological effect of liquid crystals, Nano Energy 47 (2018) 43-50.

[23] M. Liu, M. Xia, R. Qi, Q. Ma, M. Zhao, Z. Zhang, X. Lu, Lyotropic Liquid Crystal as an Electrolyte Additive for Suppressing Self-Discharge of Supercapacitors, ChemElectroChem 6(9) (2019) 2531-2535.

[24] X. Ming, L. Shi, H. Zhu, Q. Zhang, Stretchable, Phase-Transformable Ionogels with Reversible Ionic Conductor–Insulator Transition, Advanced Functional Materials 30(49) (2020) 2005079.

[25] Q. Dou, L. Liu, B. Yang, J. Lang, X. Yan, Silica-grafted ionic liquids for revealing the respective charging behaviors of cations and anions in supercapacitors, Nature communications 8(1) (2017) 1-9.

[26] J. Feng, Y. Wang, Y. Xu, H. Ma, G. Wang, P. Ma, Y. Tang, X. Yan, Construction of Supercapacitor-Based Ionic Diodes with Adjustable Bias Directions by Using Poly (ionic liquid) Electrolytes, Advanced Materials 33(31) (2021) 2100887.

[27] K. Karuppasamy, J. Theerthagiri, D. Vikraman, C.-J. Yim, S. Hussain, R. Sharma, T. Maiyalagan, J. Qin, H.-S. Kim, Ionic liquid-based electrolytes for energy storage devices: A brief review on their limits and applications, Polymers 12(4) (2020) 918.

[28] S.T.C.L. Ndruru, S. Widiarto, E. Pramono, D. Wahyuningrum, B. Bundjali, I.M. Arcana, The Influences of [EMIm] Ac Ionic Liquid for The Characteristics of Li-ion Batteries Solid Biopolymer Blend Electrolyte Based on Cellulose Derivatives of MC/CMC Blend, Macromolecular Chemistry and Physics (2022) 2100362.

[29] X. Chu, X. Zhao, Y. Zhou, Y. Wang, X. Han, Y. Zhou, J. Ma, Z. Wang, H. Huang, Z. Xu, An ultrathin robust polymer membrane for wearable solid-state electrochemical energy storage, Nano Energy 76 (2020) 105179.

[30] Y. Wang, X. Chu, Z. Zhu, D. Xiong, H. Zhang, W. Yang, Dynamically evolving 2D supramolecular polyaniline nanosheets for long-stability flexible supercapacitors, Chemical Engineering Journal 423 (2021) 130203.

[31] B. Anothumakkool, A. Torris AT, S. Veeliyath, V. Vijayakumar, M.V. Badiger, S. Kurungot, High-performance flexible solid-state supercapacitor with an extended nanoregime interface through in situ polymer electrolyte generation, ACS applied materials & interfaces 8(2) (2016) 1233-1241.

[32] C. Lei, F. Markoulidis, Z. Ashitaka, C. Lekakou, Reduction of porous carbon/Al contact resistance for an electric double-layer capacitor (EDLC), Electrochimica acta 92 (2013) 183-187.

[33] B.-A. Mei, O. Munteshari, J. Lau, B. Dunn, L. Pilon, Physical interpretations of Nyquist plots for EDLC electrodes and devices, The Journal of Physical Chemistry C 122(1) (2018) 194-206.

[34] Q. Xue, H. Gan, Y. Huang, M. Zhu, Z. Pei, H. Li, S. Deng, F. Liu, C. Zhi, Boron element nanowires electrode for supercapacitors, Advanced Energy Materials 8(20) (2018) 1703117.

[35] S.H. Mujawar, S.B. Ambade, T. Battumur, R.B. Ambade, S.-H. Lee, Electropolymerization of polyaniline on titanium oxide nanotubes for supercapacitor application, Electrochimica Acta 56(12) (2011) 4462-4466.

[36] M. Gao, X. Wu, H. Qiu, Q. Zhang, K. Huang, S. Feng, Y. Yang, T. Wang, B. Zhao, Z. Liu, Reduced graphene oxide-mediated synthesis of Mn 3 O 4 nanomaterials for an asymmetric supercapacitor cell, RSC advances 8(37) (2018) 20661-20668.

[37] B. Liu, J. Chen, B. Yang, Z. Lin, C.J. Zhang, Z. Zeng, M. Jiao, L. Liu, Y. Sun, R. Hou, An ultrahigh-energy-density lithium metal capacitor, Energy Storage Materials 42 (2021) 154-163.

[38] S. Guo, K. Zhao, Z. Feng, Y. Hou, H. Li, J. Zhao, Y. Tian, H. Song, High performance liquid crystalline bionanocomposite ionogels prepared by in situ crosslinking of cellulose/halloysite nanotubes/ionic liquid dispersions and its application in supercapacitors, Applied Surface Science 455 (2018) 599-607.

[39] T.J. Trivedi, D. Bhattacharjya, J.S. Yu, A. Kumar, Functionalized agarose self-healing ionogels suitable for supercapacitors, ChemSusChem 8(19) (2015) 3294-3303.

[40] J. Wu, G. Xia, S. Li, L. Wang, J. Ma, A flexible and self-healable gelled polymer electrolyte based on a dynamically cross-linked PVA ionogel for high-performance supercapacitors, Industrial & Engineering Chemistry Research 59(52) (2020) 22509-22519.

[41] N. Yadav, N. Yadav, S. Hashmi, Ionic liquid incorporated, redox-active blend polymer electrolyte for high energy density quasi-solid-state carbon supercapacitor, Journal of Power Sources 451 (2020) 227771.

[42] C.-L. Geng, L.-Q. Fan, C.-Y. Wang, Y.-L. Wang, S.-J. Sun, Z.-Y. Song, N. Liu, J.-H. Wu, High energy density and high working voltage of a quasi-solid-state supercapacitor with a redox-active ionic liquid added gel polymer electrolyte, New Journal of Chemistry 43(47) (2019) 18935-18942.

[43] M. Karnan, A.K. Raj, K. Subramani, S. Santhoshkumar, M. Sathish, The fascinating supercapacitive performance of activated carbon electrodes with enhanced energy density in multifarious electrolytes, Sustainable Energy & Fuels 4(6) (2020) 3029-3041.

[44] Y. Xie, Y. Liu, Y. Zhao, Y.H. Tsang, S.P. Lau, H. Huang, Y. Chai, Stretchable all-solid-state supercapacitor with wavy shaped polyaniline/graphene electrode, Journal of Materials Chemistry A 2(24) (2014) 9142-9149.

[45] T. Tevi, A. Takshi, Modeling and simulation study of the self-discharge in supercapacitors in presence of a blocking layer, Journal of Power Sources 273 (2015) 857-862.

[46] B.E. Conway, W. Pell, T. Liu, Diagnostic analyses for mechanisms of self-discharge of electrochemical capacitors and batteries, Journal of Power Sources 65(1-2) (1997) 53-59.

[47] B. Ricketts, C. Ton-That, Self-discharge of carbon-based supercapacitors with organic electrolytes, Journal of power sources 89(1) (2000) 64-69.

[48] Z. Wang, X. Chu, Z. Xu, H. Su, C. Yan, F. Liu, B. Gu, H. Huang, D. Xiong, H. Zhang, Extremely low self-discharge solid-state supercapacitors via the confinement effect of ion transfer, Journal of Materials Chemistry A 7(14) (2019) 8633-8640.

[49] Z. Wang, Z. Xu, H. Huang, X. Chu, Y. Xie, D. Xiong, C. Yan, H. Zhao, H. Zhang, W. Yang, Unraveling and Regulating Self-Discharge Behavior of Ti3C2T x MXene-Based Supercapacitors, ACS nano 14(4) (2020) 4916-4924.

[50] L. Hess, N. Fulik, J. Röhner, E. Zhang, S. Kaskel, E. Brunner, A. Balducci, The role of diffusion processes in the self-discharge of electrochemical capacitors, Energy Storage Materials 37 (2021) 501-508.

[51] A. Lewandowski, P. Jakobczyk, M. Galinski, M. Biegun, Self-discharge of electrochemical double layer capacitors, Physical Chemistry Chemical Physics 15(22) (2013) 8692-8699.

[52] M. Haque, Q. Li, C. Rigato, A. Rajaras, A.D. Smith, P. Lundgren, P. Enoksson, Identification of self-discharge mechanisms of ionic liquid electrolyte based supercapacitor under high-temperature operation, Journal of Power Sources 485 (2021) 229328.

[53] L.-Q. Fan, Q.-M. Tu, C.-L. Geng, J.-L. Huang, Y. Gu, J.-M. Lin, Y.-F. Huang, J.-H. Wu, High energy density and low self-discharge of a quasi-solid-state supercapacitor with carbon nanotubes incorporated redox-active ionic liquid-based gel polymer electrolyte, Electrochimica Acta 331 (2020) 135425.

[54] M. Haras, T. Skotnicki, Thermoelectricity for IoT–A review, Nano Energy 54 (2018) 461-476.

[55] L. Lu, W. Ding, J. Liu, B. Yang, Flexible PVDF based piezoelectric nanogenerators, Nano Energy 78 (2020) 105251.

[56] Y. Lee, S.H. Cha, Y.-W. Kim, D. Choi, J.-Y. Sun, Transparent and attachable ionic communicators based on self-cleanable triboelectric nanogenerators, Nature communications 9(1) (2018) 1-8.

[57] Z. Tian, S. Lee, G. Chen, Comprehensive review of heat transfer in thermoelectric materials and devices, Annual review of heat transfer 17 (2014).

[58] H.J. Goldsmid, Bismuth telluride and its alloys as materials for thermoelectric generation, Materials 7(4) (2014) 2577-2592.

[59] B. Chen, Q. Chen, S. Xiao, J. Feng, X. Zhang, T. Wang, Giant negative thermopower of ionic hydrogel by synergistic coordination and hydration interactions, Science advances 7(48) (2021) eabi7233.

[60] D. Zhao, A. Würger, X. Crispin, Ionic thermoelectric materials and devices, Journal of Energy Chemistry 61 (2021) 88-103.

[61] W. Liu, X. Qian, C.-G. Han, Q. Li, G. Chen, Ionic thermoelectric materials for near ambient temperature energy harvesting, Applied Physics Letters 118(2) (2021) 020501.

[62] B. Yu, J. Duan, H. Cong, W. Xie, R. Liu, X. Zhuang, H. Wang, B. Qi, M. Xu, Z.L. Wang, Thermosensitive crystallization–boosted liquid thermocells for low-grade heat harvesting, Science 370(6514) (2020) 342-346.

[63] J. Duan, B. Yu, K. Liu, J. Li, P. Yang, W. Xie, G. Xue, R. Liu, H. Wang, J. Zhou, PN conversion in thermogalvanic cells induced by thermo-sensitive nanogels for body heat harvesting, Nano Energy 57 (2019) 473-479.

[64] J. Park, J.-Y. Sun, Phase-Transitional Ionogel-Based Supercapacitors for a Selective Operation, ACS Applied Materials & Interfaces (2022).

[65] M.A. Buckingham, S. Zhang, Y. Liu, J. Chen, F. Marken, L. Aldous, Thermogalvanic and Thermocapacitive Behavior of Superabsorbent Hydrogels for Combined Low-Temperature Thermal Energy Conversion and Harvesting, ACS Applied Energy Materials 4(10) (2021) 11204-11214.

[66] V. Zinovyeva, S. Nakamae, M. Bonetti, M. Roger, Enhanced thermoelectric power in ionic liquids, ChemElectroChem 1(2) (2014) 426-430.

[67] H. Zhou, T. Yamada, N. Kimizuka, Thermo-electrochemical cells empowered by selective inclusion of redox-active ions by polysaccharides, Sustainable Energy & Fuels 2(2) (2018) 472-478.

[68] G. Laus, G. Bentivoglio, H. Schottenberger, V. Kahlenberg, H. Kopacka, T. Röder, H. Sixta, Ionic liquids: current developments, potential and drawbacks for industrial applications, Lenzinger Berichte 84(1) (2005) 71-85.

[69] P.A. Gilbert, W. Haeberli, Experiments on subtractive color mixing with a spectrophotometer, American Journal of Physics 75(4) (2007) 313-319.

[70] A. Arof, S. Amirudin, S. Yusof, I. Noor, A method based on impedance spectroscopy to determine transport properties of polymer electrolytes, Physical Chemistry Chemical Physics 16(5) (2014) 1856-1867.

Abstract in Korean

초록

사회와 산업의 급속한 발전으로 전례 없는 에너지에 대한 수요가 증가하면서, 수요에 맞게 에너지를 공급하기 위해 다양한 형태의 에너지 공급 방식이 연구되고 있다. 먼저, 에너지 저장 시스템 (ESS)은 주로 다량의 에너지가 요구되는 분야에 주로 적용되는 충전/방전 방식의 에너지 공급 장치이다. 대표적인 ESS 로는 슈퍼커패시터가 있다. 슈퍼커패시터의 전해질로 사용되는 이온 용액에서, 충전시 전기 이중층이 형성되어 에너지가 저장된다. 다음으로는, 상대적으로 적은 에너지가 필요하지만, 지속적인 에너지 공급이 필요한 분야에 적용되는 자가 발전식 에너지 공급장치이다. 이온 열전 소자가 전형적인 자가 발전식 에너지 공급 장치 이다. 열전은 양 전극에서 온도 구배에 의한 이온 농도 차이가 발생하면서 형성되는 에너지이다. 그러나, 이러한 디바이스에 적용되는 이온 용액은 보통 증발과 화학 안정에 대한 문제점을 갖고 있다. 따라서, 화학적으로 안정하고, 매우 낮은 증기압을 갖는 아이오닉 리퀴드가 차세대 물질로 주목 받고 있다.

이 논문에서 우리는 아이오닉 리퀴드를 슈퍼커패시터와 열전 소자의 전해질로 도입하여 차세대 물질로서의 효용을 증명한다. 특히, 상변화성

아이오닉 리퀴드를 기반으로한 전해질을 통해 녹는점에서 이온 전도성을 극적으로 조절할 수 있게 된다. 이러한 전해질은 새로운 기능을 갖거나 향상된 성능을 보이는 디바이스를 제작할 수 있게 한다.

제 1 부에서는, 상 변화성 아이오노젤을 전해질로 하는 슈퍼커패시터를 제작하여 선택적으로 작동되는 슈퍼커패시터를 제작한다. 슈퍼커패시터는 아이오닉 리퀴드를 젤화를 통해 매우 물리적으로 안정함을 보였다. 아이오닉 리퀴드의 상 변화성 특징은 작동 모드와 보관 모드를 구별하여 선택적으로 작동할 수 있게 하였다. 게다가 슈퍼커패시터의 단점으로 알려진 자가 방전을 보관 모드를 통해 효과적으로 억제하여 오랜 기간 보관할 수 있는 것을 보였다. 선택적으로 작동되는 슈퍼커패시터는 사막과 우주와 같은 높은 온도와 큰 온도차이를 보이는 환경에서 활용 가능 할 것으로 기대한다.

제 2 부에서는, 상 변화성 아이오닉 리퀴드를 이용하여 이온 열전 소자의 제벡 계수가 증가됨을 확인하였다. 양 전극에서 상 변화에 의한 열전 현상의 메커니즘이 소개되었다. 기존에는 물질의 고유 특성으로 알려진 제벡 계수가, 상 변화로 인해 바뀌고 phase 의 차이로 인해 높은 열전 효과 값이 도출되는 것이 확인되었다. 또한, 모든 다른 상 변화성 아이오닉 리퀴드에 대해서도 상 차이로 인해 제벡 계수가 강화됨을 증명하였다. 상 변화에 의해 강화된 열전 소자는 아직 초기단계인 열전

효과 강화에 대한 연구에 새로운 메커니즘을 제시함으로써 열전소자의 상용화를 앞당겼다고 기대한다.

Keyword : 상변화 , 아이오닉 리퀴드, 슈퍼커패시터, 열전소자

Student Number : 2016-26947

감사의 글

2012 년, 처음 서울대학교에 학부생으로 입학하고 어느 덧 10 년이란 시간이 흘렀습니다. 분에 넘치는 기회를 얻어 입학한 학교의 학부 생활은 즐겁고 스스로 배우는 것에 대한 기쁨을 느낄 수 있는 장이었습니다. 그렇게 학부 생활을 통해 얻은 지식과 경험을 오롯이 나의 것으로 발전시키기 위해 진학한 대학원은 결코 녹록지 않았습니다. 특히 연구 생활은 혼자만의 힘으로는 도저히 진행할 수 없는, 자칫하면 끝없는 방황의 길이 될 수도 있는 길이었습니다. 불안정한 저를 이렇게 학위 과정을 무사히 마칠 수 있도록 방향을 제시해주고, 이끌어주고, 함께 걸어가준 많은 분들께 10 년의 공부와 연구 성과의 길의 끝자락에서 짧게나마 감사의 인사를 전해드리고자 합니다.

먼저, 지도교수님이신 선정윤 교수님께 감사의 말씀을 드립니다. 2015 년, 학부 과정 중 무의미하게 느껴지는 공부와 미래에 대한 막연한 두려움에 사로잡혀 있을 때 무심코 찾아 뵌 오피스에서의 첫 지도로, 그때부터 '연구자'로의 길을 선택할 수 있었습니다. 그렇게 진학한 대학원에서 교수님의 지도 하에 원하는 연구를 자유롭게 진행하여 한 명의 연구자와 지성을 갖춘 인격체로서 성장할 수 있게 된 것은 두 번 다신 얻을 수 없는 행운이자 큰 기쁨이었습니다. 성심 성의껏 지도해주시고, 6 년간 웃으면서 누구보다 앞에서 이끌어주신 교수님께, 제가

연구실의 일원으로서 연구실에 더욱 큰 기여를 하지 못하고 떠남에 죄송한 마음입니다. 제가 어느 자리에서든 저희 연구실을 자랑스럽게 말하고 다닐 수 있는 것은 누구보다 교수님께서 저희 연구실에 주신 영향이라 생각하고, 즐겁게 오피스 생활을 영위해 나갈 수 있었습니다. 교수님께 다시 한 번 감사드리며, 저도 언제나 자랑스럽게 MFSM 의 일원이었음을 새기면서 부끄럽지 않은 삶을 살도록 노력하겠습니다.

오랜 시간 함께 해준 친구들 및 지인들께 감사의 인사를 전합니다. 힘들 때마다 누구보다 먼저 어깨를 걸어준 길게는 초등학교부터, 짧게는 학부 때부터 연을 계속 이어주고 있는 소중한 인연들. 얼마나 감사의 인사를 전해야 할지 모를 정도로 많은 도움을 받고 값진 추억을 준 여러분들께, 지금은 대부분 각자의 자리에서 자신의 길을 걷고 있지만 언제든 잠시 교차로에서 만나 잠시나마 회포를 풀고 다시 웃으며 헤어질 수 있길 바라고 항상 응원합니다. 또한 오랜 기간 바로 옆에서 지지해주고 행복한 시간과 추억을 쌓아준 지현이에게 감사합니다. 새롭게 열릴 상황과 시간 속에서 앞으로도 함께 어려움은 두 손 꼭 잡은 채 극복해 나아가고 즐거움은 공유하며 좋은 추억 쌓아가도록 합시다. 모든 일에 축복하고 항상 좋은 일만 발생하길 기원합니다.

6 년간 어떠한 사람보다 시간적으로 많은 교류를 가졌던 우리 MFSM 의 인원들께도 감사의 말씀을 전합니다. 먼저 MFSM 의 든든한

맏형인 김용우 형, 항상 쾌활한 성수형, 젠틀한 강용우형, 제 첫 연구 메이트이자 항상 긍정적이신 창서형, 부드럽게 연구 지도해주신 수호형, 항상 잘 챙겨주신 호준이형, 언제나 멋있게 사시는 혜원누나, 꽃 길만 남은 재호형, 학부 때부터 든든한 순보, 연구와 먼저 결혼한 재만이, 만능인 현재, 연구와 결혼 다 잡은 현욱(과 창서형), 옆자리에서 잘 놀아준 기민이, 즐거운 민규, 즐겁게 대화 이끌어준 마가, 연구 기둥 원준이, 열심히 하는 만큼 잘 되었으면 하는 솔지, 노력과 실력 다 갖춘 윤혁이, 연구가 기대되는 시환이, 은은하지만 잘 하는 성유, 용머든 용은, 쾌남 병익이까지 항상 감사했고, 모두 훌륭한 연구자가 되기를 바랍니다.

마지막으로, 항상 지지와 응원을 아끼지 않은 우리 가족 감사하고 사랑합니다. 남들보다 훨씬 오래한 학업 기간 동안 누구보다 힘드셨음에도 불구하고 곁에서 지지해주시고 응원해주신 아버지, 어머니 그리고 형, 당신들 덕분에 힘든 시간 속에서도 행복했고, 무사히 학위를 마칠 수 있었습니다. 항상 그립고 사랑합니다. 새로운 환경과 생활 속에서도 가족이라는 매듭으로 단단하게 묶여 힘든 시간에서는 서로를 지탱하고 즐거운 시간속에서는 계속해서 추억을 쌓을 수 있도록, 그리고 행복한 시간만이 가득했으면 좋겠고 저 또한 응원합니다.

2022 년 8 월

박 진 우 올림.